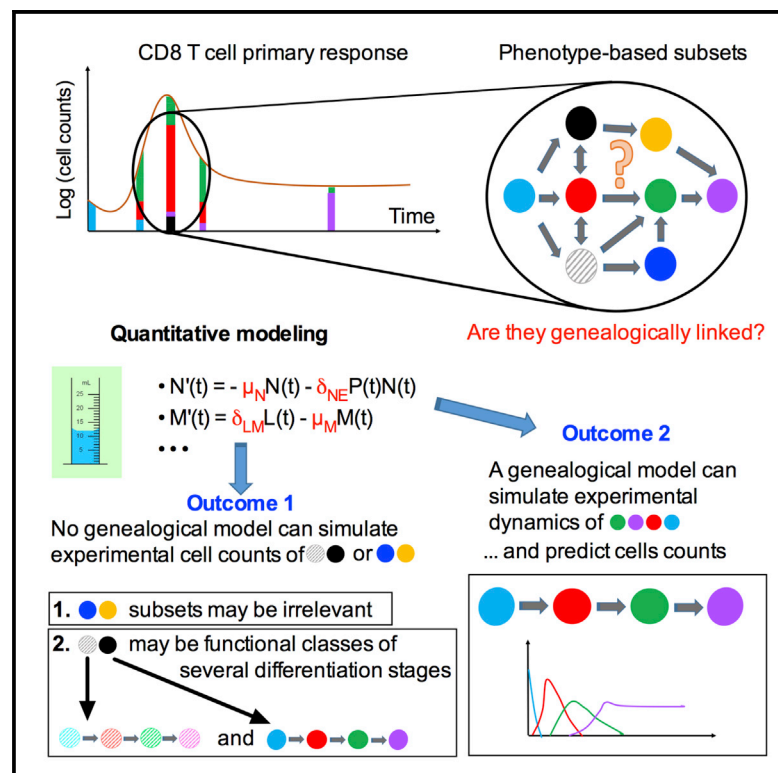# Cell Systems

Identification of Nascent Memory CD8 T Cells and Modeling of Their Ontogeny

Graphical Abstract

Authors

Fabien Crauste, Julien Mafille,
Lilia Boucinha, Sophia Djebali,
Olivier Gandrillon, Jacqueline Marvel,
Christophe Arpin

Correspondence

jacqueline.marvel@inserm.fr (J.M.),
christophe.arpin@inserm.fr (C.A.)

In Brief

Phenotypic identification of nascent memory CD8 T cells during a primary response and mathematical modeling allows the delineation of memory cell ontogeny and early prediction of long-term protective memory cell counts.

Highlights

- Phenotypic identification of nascent memory cells

- Mathematical models of cell-count dynamics delineate naive to memory cell genealogy

- In silico prediction of long-term memory cell counts from a few early measurements

CellPress

Article

Identification of Nascent Memory CD8 T Cells and Modeling of Their Ontogeny

Fabien Crauste,[1,2,5] Julien Mafille,[3,5,6] Lilia Boucinha,[3,7] Sophia Djebali,[3] Olivier Gandrillon,[1,4] Jacqueline Marvel,[3,*] and Christophe Arpin[3,8,*]

[1]Team Dracula, Inria, 69603 Villeurbanne, France
[2]Institut Camille Jordan, Université de Lyon, Université Claude Bernard Lyon 1, CNRS UMR 5208, 43 Boulevard du 11 novembre 1918, 69622 Villeurbanne Cedex, France
[3]CIRI, ICL, INSERM U1111, Université Claude Bernard Lyon 1, CNRS UMR 5308, École Normale Supérieure de Lyon, Université de Lyon, 69007 Lyon, France
[4]Laboratory of Biology and Modelling of the Cell, Université de Lyon, ENS de Lyon, Université Claude Bernard, CNRS UMR 5239, INSERM U1210, 46 allée d'Italie Site Jacques Monod, 69007 Lyon, France
[5]Co-first author
[6]Present address: Myltenyi Biotec, 75011 Paris, France
[7]Present address: MaaT Pharma, 69007 Lyon, France
[8]Lead Contact
*Correspondence: jacqueline.marvel@inserm.fr (J.M.), christophe.arpin@inserm.fr (C.A.)
http://dx.doi.org/10.1016/j.cels.2017.01.014

SUMMARY

Primary immune responses generate short-term effectors and long-term protective memory cells. The delineation of the genealogy linking naive, effector, and memory cells has been complicated by the lack of phenotypes discriminating effector from memory differentiation stages. Using transcriptomics and phenotypic analyses, we identify Bcl2 and Mki67 as a marker combination that enables the tracking of nascent memory cells within the effector phase. We then use a formal approach based on mathematical models describing the dynamics of population size evolution to test potential progeny links and demonstrate that most cells follow a linear naive→early effector→late effector→memory pathway. Moreover, our mathematical model allows long-term prediction of memory cell numbers from a few early experimental measurements. Our work thus provides a phenotypic means to identify effector and memory cells, as well as a mathematical framework to investigate their genealogy and to predict the outcome of immunization regimens in terms of memory cell numbers generated.

INTRODUCTION

Primary antigenic insult by a pathogen or a tumor leads to the activation of rare naive CD8 T cells that, under appropriate conditions, expand tremendously and differentiate into cytotoxic effectors, eliminating pathogen-infected or tumor cells. Eventually, the primary response terminates, leaving a most potent long-lived memory population that rapidly protects in the event of a subsequent re-encounter with the same antigen. Induction of memory cells is the goal of vaccination, and understanding the process leading to their generation is thus important in that context. Moreover, because the process of memory development spans several weeks, the early ability to predict the number of memory cells generated after an immunization would facilitate the screening of candidate vaccines.

In the past decades, considerable work has been performed to identify the cellular transition stages between naive and memory cells, to delineate their genealogy and to highlight the molecular processes and controllers that could be targeted for immuno-intervention (Chang et al., 2014; Harty and Badovinac, 2008; Kaech and Cui, 2012).

Two major antigen-primed populations emerge from naive precursors: effectors that ensure immediate defense and eradication of the pathogen and a long-term protective memory population. Both can be distinguished from naive cells based on their phenotype, as the expression of a few surface markers (for example, CD44, CCL5, and CXCR3) is modified early after antigen encounter. However, this modified expression is maintained throughout the effector and memory stages and is thus inappropriate to identify memory cells that are generated during the ongoing effector phase.

A number of other surface markers (CCR7, CD62L, KLRG1, CD27, CD127, and CD28) that are only modified by a fraction of effector or memory cells have been used alone or in combinations to classify these antigen-primed cells into multiple subsets that differ in some of their functional properties or in their memory generation potential (Appay et al., 2008; Buchholz et al., 2013; Chang et al., 2014; Jameson et al., 2015; Kaech and Cui, 2012; Masopust et al., 2001; Sallusto and Lanzavecchia, 2001). Defining the lineage relationship between these subsets is a key element in our comprehension of the memory generation process. However, it does remain controversial (Ahmed et al., 2009; Arsenio et al., 2015; Flossdorf et al., 2015; Kaech and Cui, 2012). Indeed, putative genealogies were proposed from non-quantitative approaches, such as transfer experiments that identify populations enriched in precursors of given differentiation stages or molecular (transcriptome or T cell receptor [TCR] repertoire) analyses that identify
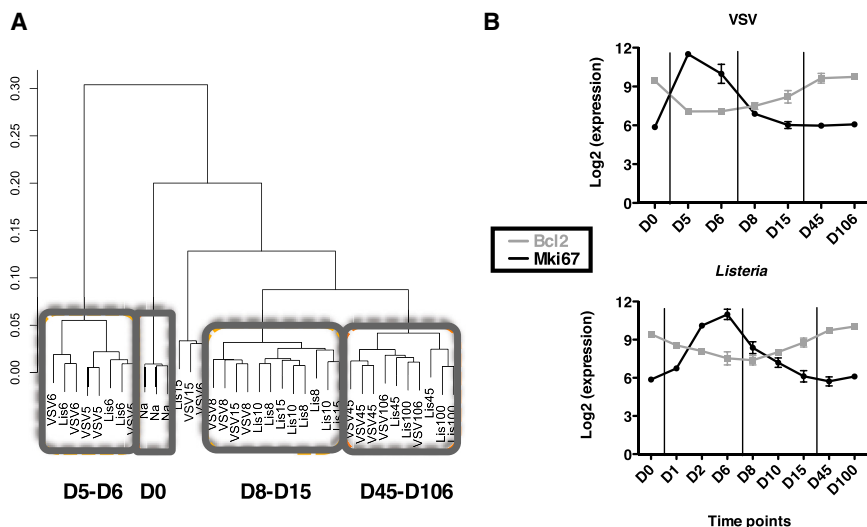
Figure 1. Analysis of Longitudinal Transcriptomics Data of Murine Primary CD8 T Cell Responses from the Immunological Genome Project Consortium

Transcriptomics data from spleen OT-I CD8 T cells at D0–D106 after VSV-OVA, and at D0–D100 after Lis-OVA infections, were clustered for similarities in (A) and analyzed by a top score pair approach in (B).

(A) Similarity analysis identifies four clusters corresponding to naive, D5–D6, D8–D15, and D45–D106 responders.

(B) Bcl2 (gray) and Mki67 (black) relative expression levels (means ± SEM) during the course of a response to VSV (upper graph) and *Listeria* (lower graph). Vertical bars mark boundaries between naive, early effector, late effector, and memory phases, as determined by the clustering in (A).

See also Figures S1 and S4 and Table S1.

clonotypic families. For instance, the genealogical link between CD62L+ central (T$_{CM}$) and CD62L– effector (T$_{EM}$) memory T cells, the two first subsets that were described in humans and mice (Masopust et al., 2001; Sallusto et al., 1999), has been the purpose of multiple studies. The generation of T$_{EM}$ from primary T$_{CM}$ after repetitive stimulation and/or strong antigenic and inflammatory signals was proposed (Kaech and Cui, 2012), while the inversed relation, i.e., the generation of T$_{CM}$ from T$_{EM}$ has also been reported (Wherry et al., 2003). Moreover, based on their TCR repertoire it was suggested that T$_{CM}$ and T$_{EM}$ could represent separate developmental lineages (Baron et al., 2003; Bouneaud et al., 2005).

More recently, CD127/KLRG1 expression has been used to identify memory precursor cells (MPECs) during the effector phase and the genealogical links between CD127/KLRG1-defined effector subsets have been defined by transfer experiments (Joshi et al., 2007). Results showed that CD127– KLRG1– early effector cells give birth to both CD127– KLRG1+ short-lived effector cells (SLECs), a terminally differentiated population destined to die, and CD127+ KLRG1– MPECs (Kaech and Cui, 2012; Plumlee et al., 2015). This large MPEC population present at the peak of the response does not, however, strictly correspond to the memory population as it is molecularly heterogeneous, containing both effector cells and memory precursors cells (Arsenio et al., 2014; Hand et al., 2007).

Herein, we revisited this question with a quantitative modeling framework to establish a genealogy between phenotypically defined subsets by assessing putative differentiation schemes in their ability to simulate population count dynamics. We first identify Bcl2 and Mki67 as phenotypic markers distinguishing between co-existing effector and memory populations and allowing the identification of nascent memory cells within the heterogeneous MPEC population. Using mathematical modeling, we demonstrate that the majority of cells follow a linear naive → early effector → late effector → memory differentiation pathway. This pathway can be followed by both central CD62L+ and effector CD62L– lineages. Furthermore, we show that only a few early experimental measurements suffice to

determine the parameter values of the mathematical model and to allow simulation of subset dynamics to predict long-term memory cell counts.

RESULTS

Transcriptome Analyses Reveal the Existence of Two Differentiation Stages during the Effector Phase

To identify discriminative phenotypes between effector and memory CD8 T cells, we sought molecules specifically expressed at given differentiation stages during a primary CD8 T cell response. To do this, we made use of transcriptomics data published by the Immunological Genome Project Consortium (GEO: GSE15907, www.immgen.org/) (Best et al., 2013). These data encompass transcriptome analyses of OT-I mouse TCR-transgenic (TCR-tg) CD8 T cells from naive to memory stages following ovalbumin (OVA)-expressing *Listeria* (Lis-OVA) and vesicular somatitis virus (VSV-OVA) infections. A similarity-based hierarchical clustering identified four groups of gene expression patterns corresponding to naive, day 5 to day 6 (D5-D6), D8-D15, and D45-D106 responders for both bacterial and viral immunizations (Figure 1A). Thus, the effector phase seems to part in two stages, one early (D5-D6) and one late (D8-D15).

We then looked for pairs of genes that display the most opposite expression patterns along the kinetics, using a top-scoring pair approach (Geman et al., 2004). Among these, a number of pairs was identified with a strong expression of molecules notably associated with the cell cycle during the early stage of the effector phase (Figure S1). Of note, the widely used proliferation marker Mki67 (Starborg et al., 1996) is expressed by effector but not by memory antigen-specific CD8 T cells in humans following yellow fever and smallpox vaccine administration, while Bcl-2 expression is conversely restricted to the memory population (Miller et al., 2008). We thus looked at the pattern of Mki67 and Bcl2 expression by CD8 T cells during the course of a primary response in mice. Transcripts encoding Mki67 are strongly induced during the

early stage of the effector phase in response to VSV-OVA or Lis-OVA, while Bcl2 expression is downregulated along both effector phases (Figure 1B). In conclusion, data from the literature (Miller et al., 2008) and expression databases (Best et al., 2013) indicate a biphasic effector stage and suggest that Bcl2 and Mki67 could help to distinguish between effector and memory cells.

Mki67/Bcl2 Co-expression Patterns Define Two Effector and One Memory Cell Populations

We thus investigated Mki67/Bcl2 co-expression by CD8 T cells during a primary response, in combination with CD44 expression that rapidly upregulates upon activation and thus distinguishes between naive and antigen-primed cells. To do this, C57BL/6 mice were transferred with naive CD8 T cells from F5 TCR-tg mice and subsequently immunized by intranasal infection with an NP68-expressing vaccinia virus (VV-NP68). Immunized hosts were regularly bled and F5 CD8 T cell responders were counted and analyzed for CD44/Mki67/Bcl2 co-expression.

During the course of this response, CD44+ virus-primed F5 responders homogeneously adopted three successive phenotypes (Mki67+ Bcl2–, Mki67– Bcl2–, and Mki67– Bcl2+) as exemplified in Figure 2A. As expected, naive cells are CD44– Mki67– Bcl2+ and rapidly decline beyond the detection limit by D7 of the response (Figure 2B). Among CD44+ antigen-primed cells, F5 CD8 responders are almost exclusively Mki67+ Bcl2– between D5 and D10 of the response, Mki67– Bcl2– cells dominate the response around D15, and an Mki67– Bcl2+ population is detectable by D13 and virtually represents all cells by D30 and later on (Figure 2B). Each phase of the response, as identified by common transcriptomics signatures (Figure 1A), is thus dominated by a population specifically identified by its CD44/Mki67/Bcl2 phenotype. Furthermore, the cytolytic effector function analyzed by Granzyme B expression is mostly restricted to the CD44+ Bcl2– compartment (Figure S2A). CD44+ Bcl2+ Mki67– cells display a low level of activation (only 5% of the cells are Granzyme B+) but confer an improved protection against a lethal viral challenge (Figure S2B). CD44+ Bcl2– and CD44+ Bcl2+ Mki67– cells thus functionally define the effector and memory populations, respectively, and we can propose a sequence of subset appearance (Figure 2C), where naive and primed cells are distinguished by CD44 expression, effector and memory populations among CD44+ primed cells are discriminated by their level of Bcl2 expression, and CD44+ Bcl2– effectors are split into early Mki67+ and late Mki67– stages.

The same succession of CD44/Mki67/Bcl2-defined populations was observed in the blood (Figure 2), spleen, draining lymph nodes, and the site of infection (lung) and following a systemic intraperitoneal injection (data not shown), as well as when following the F5 CD8 T cell response to a tumor immunization (Figure 2D). Moreover, vaccinia-specific, non-TCR-tg cells identified by B8R-MHC-I multimer binding followed the same sequence of differentiation (Figure 2E). Thus, the naive→early effector→late effector→memory sequence defined here is not characteristic of TCR-tg cells or of a given immunization regimen but a general feature of murine CD8 T cell primary responses in vivo.

Mathematical Modeling Confirms the Existence of Two Effector Differentiation Stages

The differentiation scheme in Figure 2C is solely based on the successive dominance of the response by each subset. To determine the potential genealogical links between these subsets, we used mathematical modeling to evaluate the performance of putative genealogical models at reproducing the quantitative kinetics of subset cell counts. We first assessed the ability of the sets of ordinary differential equations driving the mathematical models to reproduce cell-count dynamics of B8R-specific endogenous CD8 T cells (Figure 2E). Models were ranked according to their ability to reproduce experimental dynamics (smallest χ^2 values) and a statistical test (corrected Akaike Information Criterion [AICc]) that, beyond considering the ability to minimize χ^2, penalizes over-parameterized models (Hurvich and Tsai, 1989). Details on mathematical modeling are given in the STAR Methods.

We previously established a minimal mathematical model able to simulate the dynamics of total CD8 T cells during a primary response, considering a naive→effector→memory differentiation scheme (Crauste et al., 2015; Terry et al., 2012). Given that transcriptomics data and CD44/Mki67/Bcl2 phenotypes revealed two effector phases, we modified our initial model to take into account these two compartments (Figure S3A). To allow comparison between three- and four-compartment models, early (E) and late (L) cellular compartments were summed up for both experimental and simulation results (Table S1). Cell counts of naive (N), both early and late effectors (EFF), and memory (M) compartments were then fitted simultaneously using PottersWheel MATLAB Toolbox, which fits the time series of all three subsets together. According to the AICc criterion (Table S1), which strongly penalizes over-parameterized models, both models perform equally well. However, the three-compartment N(E+L)M model poorly simulates effector (χ^2_{EFF} = 9.1) and memory (χ^2_M = 7.9) cell dynamics (Table S1 and Figure S4). Thus, mathematical modeling supports the existence of the two effector stages highlighted by expression data.

Mathematical Models Support a Linear N→E→L→M Differentiation Pathway

To assess several putative parenthood links between the four cellular compartments defined by CD44/Mki67/Bcl2 expression levels, we next compared several four-compartment models (Figure S3) and thus fitted E and L cells separately (STAR Methods). According to AICc values and Akaike weights, the linear NELM model proves to be the best model to describe the data, with a probability of 0.98 (Table 1). This is also true when the six top models presented in Figure 3A were compared with regard to their ability to fit the data, depicted in Figure 2D, of the F5 response to a tumor immunization (Table S2). Although other models have very low probabilities to be the best models, we hereafter investigate how they perform at simulating experimental data.

The linear NLEM model D and NL branching derivatives, in which naive cells first differentiate into L effectors, yielded the highest χ^2 and AICc values (Table 1). The only means to improve their ability to reproduce experimental data is to allow L cells to proliferate (data not shown), which is not in agreement with their Mki67– phenotype (Starborg et al., 1996). Among others, models in which M cells do not originate uniquely from the L
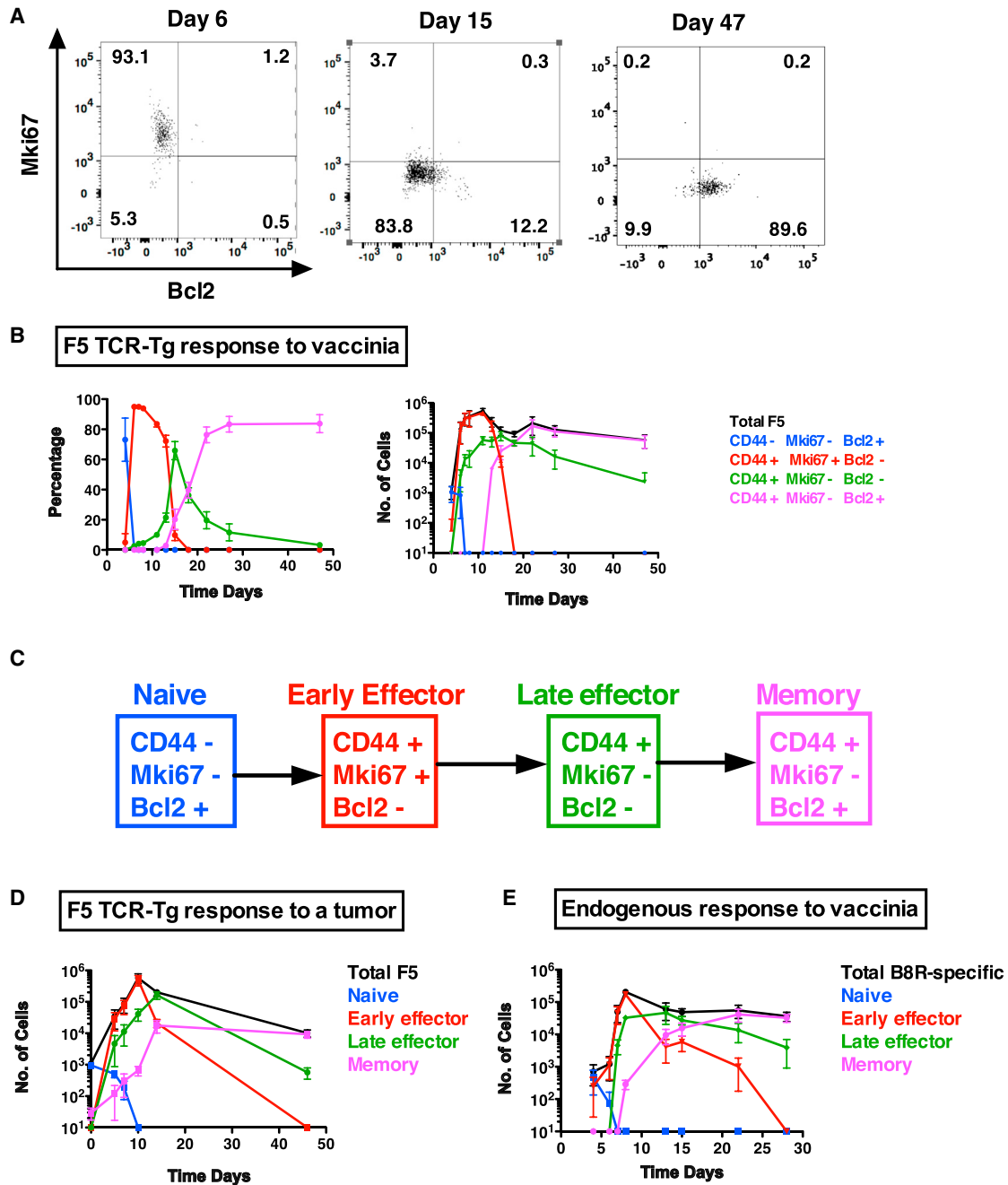
Figure 2. Identification of CD8 T Cell Differentiation Stages during a Primary Response

Naive CD45.1+ F5 TCR-tg CD8 T cells were transferred to CD45.2+ C57BL/6 congenic recipients, which were immunized the next day by intranasal infection with VV-NP68 in (A), (B), and (E) or by subcutaneous injection with the tumor EL4-NP68 in (D). At the indicated time points, recipients were bled and F5 TCR-tg in (A), (B), and (D), or endogenous B8R-specific in (E), CD8 T cell responders were identified by CD45.1 or B8R-multimer staining, respectively, and analyzed by flow cytometry for CD44/Mki67 and Bcl2 co-expression.

(A) Representative images of Mki67/Bcl2 co-expression by CD44 + F5 responders at the indicated times. Numbers represent the percentages of cells in each quadrant.

(B) Overlay of the percentages (left) and absolute numbers (right) of CD44– Mki67– Bcl2+ (blue), CD44+ Mki67+ Bcl2– (red), CD44+ Mki67– Bcl2– (green), and + Mki67– Bcl2+ (purple) subsets at the indicated times.

(C) Sequence of appearance and phenotype of the four differentiation stages identified by CD44/Mki67/Bcl2.

(D and E) Absolute cell counts of CD44/Mki67/Bcl2 defined subsets among F5 responders to an EL4-NP68 immunization (D) or endogenous B8R-specific CD8 T cell responders to a VV infection (E).

One representative experiment out of three to four, with three to five mice in each group (mean ± SD, when depicted).

See also Figures S1 and S2 and Tables S1 and S2.

Table 1. Comparative Analysis of All Four-Compartment Models

Model[a]	No. of Pars.[b]	χ^2[c]	χ^2_N	χ^2_E	χ^2_L	χ^2_M	AICc[d]	Δ_i[d]	w_i[d]
Linear Models									
(A)[e] NELM	12	**19.9**	0.1	11.9	1.8	6.1	**445**	0	**98**
(B)[e] NMEL	11	45.2	0.1	6.6	2.3	36.2	459	14	0.1
(C)[e] NMLE	9	132.0	0.1	10.5	85.0	36.4	529	84	0
(D)[e] NLEM	9	186.5	3.8	90.2	89.5	2.9	583	138	0
Branching: NEL Models									
(a)[e] NbEMbELM	13	20.0	0.1	11.9	1.8	6.2	460	15	0.05
(b)[e] bNMbNELM	13	20.2	0.1	11.9	1.9	6.3	460	15	0.05
(c)[e] bNMbN(bEMbELM)	14	20.5	0.1	12.1	1.9	6.4	481	36	0
(d)[e] NbEMbEL	13	22.0	0.1	10.7	1.7	9.5	462	17	0.02
(e)[e] bNMbN(bEMbEL)	14	22.2	0.1	10.7	2.0	9.4	482	37	0
Branching: NM Models									
(f)[e] bNMbNEL	10	49.0	0.0	10.6	2.9	35.5	453	8	1.7
(g)[e] NbMEbML	11	123.9	0.1	2.5	85.0	36.4	537	92	0
Branching: NL Models									
(h)[e] bNEMbNLM	10	170.5	0.1	47.8	88.4	34.2	575	130	0
(i)[e] bNEbNLM	10	170.7	0.1	47.8	88.4	34.4	575	130	0
(j)[e] bNEMbNL	11	180.6	3.8	89.5	86.9	0.4	594	149	0
(k)[e] bNMbNLEM	9	186.5	3.8	90.2	89.5	2.9	583	138	0
(l)[e] NbLMbLEM	10	186.5	3.8	90.2	89.5	2.9	591	146	0
(m)[e] bNMbN(bLMbLEM)	10	188.6	0.2	87.2	87.0	14.2	593	148	0

For distances between best simulations and biological data (χ^2 values) and the statistical test (AICc) the smaller the value, the better the model. Best values are shown in bold. See STAR Methods for χ^2, AICc, and w_i calculations.

[a]Schematic representations are given in Figure S3.

[b]Number of significant parameters.

[c]$\chi^2 = \chi^2_N + \chi^2_E + \chi^2_L + \chi^2_M$.

[d]AICc is for corrected Akaike Information Criterion (Hurvich and Tsai, 1989), Δ_i is the difference between the minimal value of AICc (here 445) and the value of the model; and w_i are the Akaike weights (Burnham and Anderson, 2002), in percentages.

[e]Names correspond to those given in Figure S3 and are explained in its legend. See also Figures S3 and S5 and Table S3.

compartment (linear models B and C, branching models a–g) perform much worse than the NELM model. Model f, which ranks second based on AICc and generates M cells only from N cells, is unable to fit data on M cell counts (Figure S5A). Model B, which ranks third based on AICc and assumes a linear NMEL pathway, simply does not generate any M cells (Figure S5B), and its rank is mostly due to its ability to generate dynamics at the cost of un-physiological values for parameters μ_{LE} and μ_{PE} (Table S3).

Among the six models with a probability greater than 0.01% (arbitrary threshold) to be the best model (Figure 3A), five models display the N→E→L (i.e., NEL) sequence and three models display the NELM sequence (A, a, and b). For the latter, it is noticeable that the differentiation rates of either naive ($\delta_{NM} \leq 10^{-4}$ day^{-1}) or early effectors ($\delta_{EM} \leq 10^{-3}$ day^{-1}) in memory cells are much smaller than those of late effectors ($\delta_{LM} \sim 0.025$ day^{-1}, Table S3). Thus, even though our results do not exclude the possibility of generating some memory cells directly from naive or early effectors on top of the NELM backbone, they indicate, with a very high probability, that most memory cells differentiate along the linear N→E→L→M pathway (Figure 3).

In conclusion, mathematical modeling establishes that during primary responses, naive cells (N, CD44– Mki67– Bcl2+) differentiate into proliferating early effectors (E, CD44+ Mki67+ Bcl2–) that return to quiescence as late effectors (L, CD44+ Mki67– Bcl2–), from which the majority of memory cells (M, CD44+ Mki67– Bcl2+) emerges (Figures 2C and 3B).

Subsets Defined by CD127/KLRG1, but Not by CD62L Expression Levels, Define Differentiation Stages Linked by a Genealogy

Many genealogical filiations during primary CD8 T cell responses have been proposed based on phenotypic markers (Chang et al., 2014; Harty and Badovinac, 2008; Kaech and Cui, 2012). For instance, based on the downregulation of CD62L expression on the majority of cells during the effector phase (Figure 4A), some models have proposed that CD62L+ T_{CM} memory cells are generated from CD62L– effectors or early T_{EM}. However, the extensive cellular expansion occurring during the effector phase translates into an expansion/contraction dynamics of both CD62L– and CD62L+ effectors (Figure 4A and Kedzierska et al., 2007), making it difficult not to consider that T_{CM} may originate from CD62L+ effectors. Interestingly, both CD62L+ and CD62L– cells were able to follow a complete NELM pathway, as defined by CD44/Mki67/Bcl2 co-expression (Figure 4B). Thus, although our results cannot exclude interconversions between CD62L+ and CD62L– cells, they show that T_{EM} and T_{CM} can develop as separate lineages in line with previous results (Baron et al., 2003; Bouneaud et al., 2005).
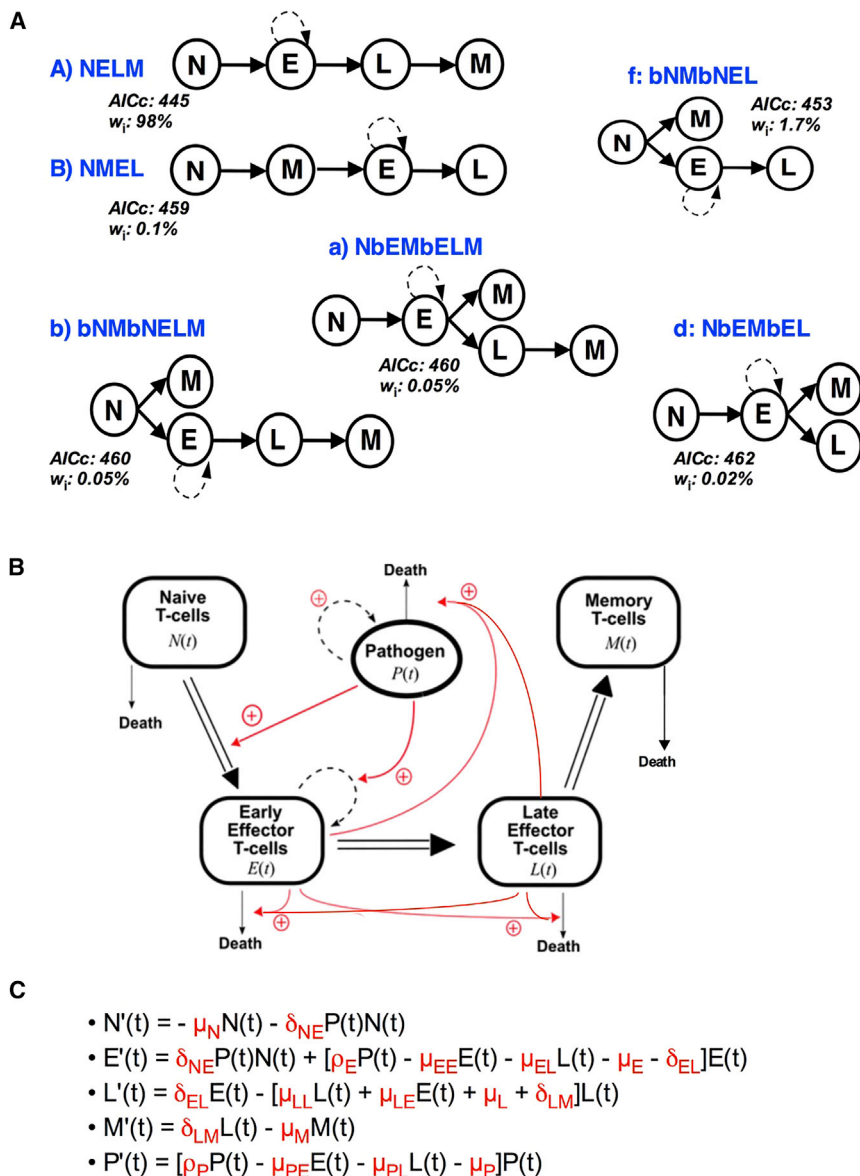
Figure 3. Best-Performing Differentiation Models

(A) Schematic version of the six top models. Differentiation pathways between N, E, L, and M cellular compartments are represented by plain arrows. Circular dotted arrows depict proliferation and red circles represent cellular compartments in the common NEL backbone. AICc and Akaike weight values are indicated for each model (See Table 1).

(B) Full description of the NELM model. The pathogen P and CD8 T cell differentiation stages are presented in boxes. Double arrows represent the differentiation paths, black arrows represent evolution to death, and the dotted black arrows represent proliferation. Positive feedback is depicted with red arrows.

(C) The set of ordinary differential equations driving the NELM model. Let $F'(t)$ be the time derivative of $F(t)$, where $F \in \{N; E; L; M; P\}$. Parameters appear in red, i.e., μ_X is the natural death rate of X cells. μ_{XY} reflects the death rate of X cells under the influence of Y cells. δ_{XY} is the differentiation rate of X cells into Y cells. ρ_X is the proliferation rate of X cells.

See also Figures S3 and S5 and Tables S2 and S3.

CD44+ Mki67– Bcl2+ Cells Represent Emerging Memory CD8 T Cells among MPEC

MPEC, although enriched in memory precursors (Joshi et al., 2007), define a heterogeneous population (Arsenio et al., 2014; Hand et al., 2007), and we thus investigated the relationships between the herein-defined NELM pathway and the SLEC/MPEC paradigm. We observed that MPEC peak and dominate the response of F5 cells at D8 (Figure 5A), as observed for P14 TCR-tg cells in response to VV (Joshi et al., 2007). However, Mki67/Bcl2/CD127/KLRG1 co-expression analyses revea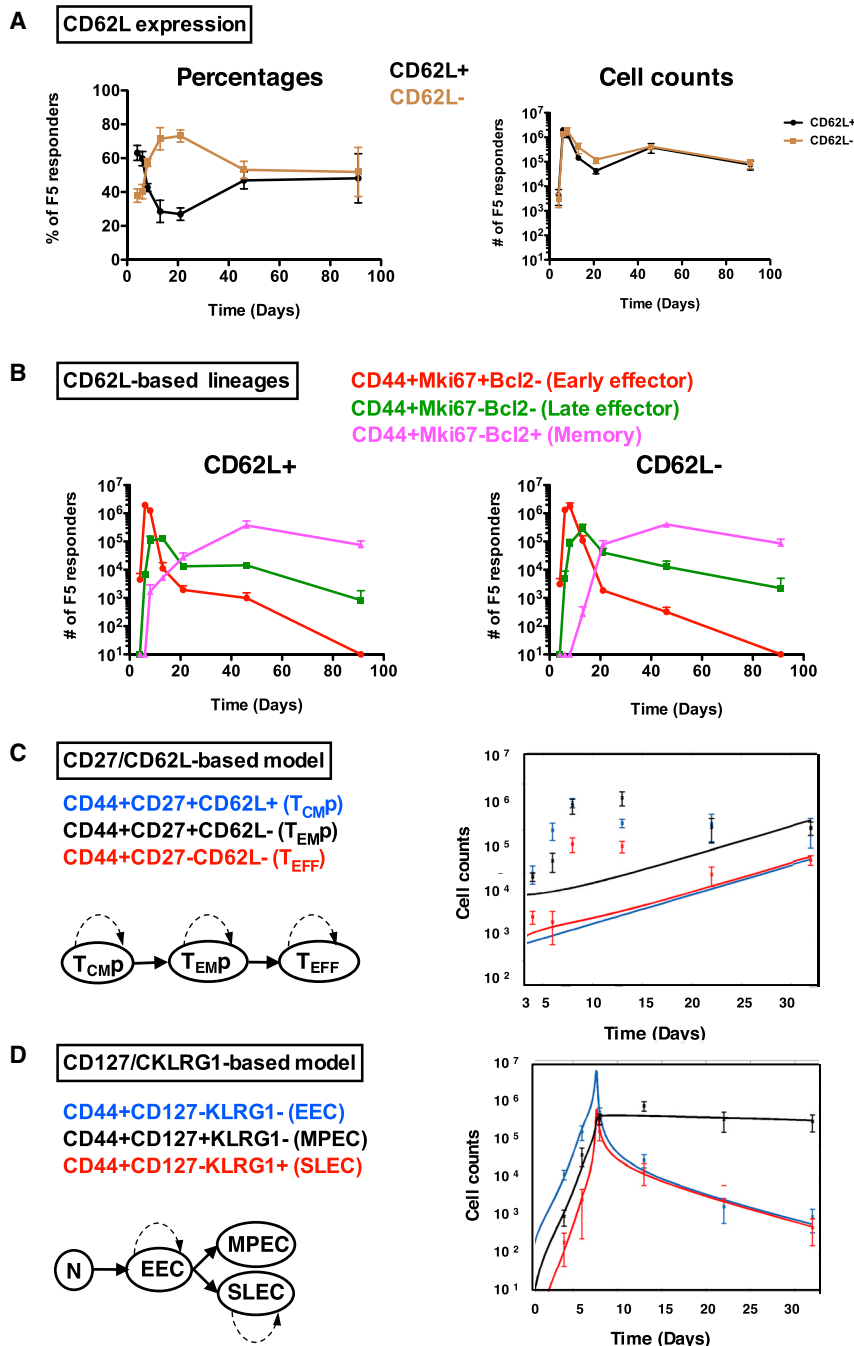led that the MPEC population was mostly composed of Mki67+ Bcl2–early effectors at D8, Mki67– Bcl2– late effectors at D13, and then slowly enriched itself in Mki67– Bcl2+ memory cells that constitute virtually all MPEC cells at D46. Thus, while contracting, the MPEC population slowly enriches itself in memory cells, as defined by their Mki67/Bcl2 phenotype (bottom line in Figure 5A). Conversely, the Mki67– Bcl2+ memory population steadily increases in size and is completely restricted to the CD127+ KLRG1– MPEC phenotype from its very appearance around D8 (bottom line in Figure 5B). Thus, the CD44+ Mki67– Bcl2+ phenotype identifies emerging memory CD8 T cells within the heterogeneous MPEC population.

The NELM Mathematical Model Can Predict Long-Term Memory Cell Counts from Early Subset Measurements

Considering the ability of our model to fit to experimental data, we next tested its capacity to achieve long-term prediction of memory cell quantities. Indeed, the first aim of vaccine

Using the CD27/CD62L expression pattern of individual OT-I TCR-tg CD8 T cells stimulated by *Listeria* in vivo, it has recently been proposed that memory cells could appear before effectors in the differentiation pathway (Buchholz et al., 2013). However, the proposed pathway, which does not harbor negative feedback loops, can reproduce the dynamics of populations in terms of relative percentages (Buchholz et al., 2013) but fails to reproduce experimental cell counts, notably their decrease after D12 of the response (Figure 4C). In conclusion, CD62L-based phenotypic definitions of CD8 T cell populations may rather represent different functional classes of cells than populations with parental relationships.

Conversely, the CD127/KLRG1-based SLEC/MPEC paradigm seems to represent a true genealogy as suggested by transfer experiments (Joshi et al., 2007) and the fact that it can be successfully described by the corresponding dynamical model (Figure 4D).

A CD62L expression

B CD62L-based lineages

CD44+Mki67+Bcl2- (Early effector)
CD44+Mki67-Bcl2- (Late effector)
CD44+Mki67-Bcl2+ (Memory)

C CD27/CD62L-based model

CD44+CD27+CD62L+ ($T_{CM}p$)
CD44+CD27+CD62L- ($T_{EM}p$)
CD44+CD27-CD62L- (T_{EFF})

D CD127/CKLRG1-based model

CD44+CD127-KLRG1- (EEC)
CD44+CD127+KLRG1- (MPEC)
CD44+CD127-KLRG1+ (SLEC)

Figure 4. Subsets Defined by CD127/KLRG1, but Not by CD62L Expression Levels Define Differentiation Stages Linked by a Genealogy

Naive CD45.1+ F5 TCR-tg CD8 T cells were transferred to CD45.2+ C57BL/6 congenic recipients, which were immunized the next day by intranasal infection with VV-NP68. At the indicated time points, spleens were collected and F5 CD8 T cell responders were analyzed by flow cytometry for: (A–C) CD27, CD62L, CD44, Mki67, and Bcl2 co-expression, to determine: (A) the percentages (left-hand graph) and absolute cell counts (right-hand graph) of CD62L+ (black curves) and CD62L− (brown curves) total F5 responders; (B) the number of early effector (red), late effector (green), and memory (purple) cells in the CD62L+ (left hand graph) and CD62L− (right hand graph) compartments; and (C) the number of TCMp (blue), TEMp (black), and TEFF (red) populations represented by points with SD error bars on the right-hand graph together with the best simulation (curves) obtained with the corresponding TCMp→TEMp→TEFF model published in Buchholz et al. (2013) and depicted on the left.

(D) CD44, CD127, and KLRG1 co-expression, to determine the number of EEC (blue), MPEC (black), and SLEC (red) populations represented by points with SD error bars on the right-hand graph together with the best simulation (curves) obtained with the corresponding N(bEEC/SLEC)(bEEC/MPEC) paradigm depicted on the left. Plain and dotted arrows represent differentiation and proliferation, respectively. The equations driving the models presented in (C) and (D) are given in the STAR Methods.
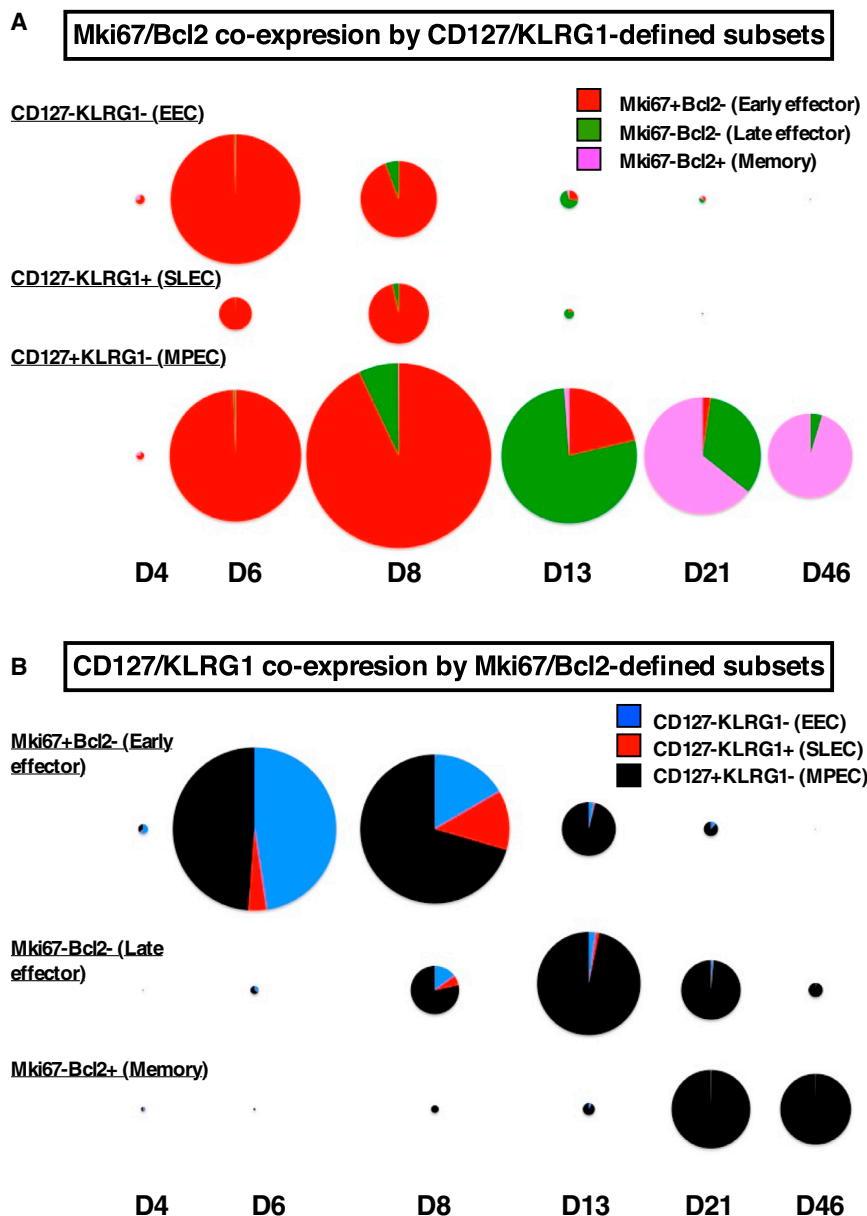
cells at the last experimental point and the number of responders at the captured time of the peak is 1.6% and 16%, respectively. Thus, applying a 5%–10% rule would have under- or overestimated the number of memory cells generated and blurred the difference between the two systems. We thus questioned whether the NELM model could help to predict the number of memory cells generated.

To do this, we used sets of experimental measures restricted to early time points to estimate the model parameter values and generate cellular dynamics that we compared with simulations obtained with all experimental data. Those included measurements at D4, D6, D7, D8, D13, D15, D22, and D28. Using only data up to D7 or D8 is not sufficient to obtain good simulations of the total CD8 and memory cell dynamics (Figures 6A and 6B) or of the effector cell subsets (Figures S6A and S6B). However, when extending the measurements up to D13, it was possible to generate simulations of total cell and subset dynamics that fit experimental results and are very similar to the simulations obtained using data from all time points (Figures 6C and S6C). Moreover, extending the measurements to D15 did not significantly

candidates is to induce as many memory CD8 T cells as possible to ensure subsequent protection. One can consider, based on lymphocytic choriomeningitis virus infection data (Badovinac et al., 2002; Murali-Krishna et al., 1998), that 5%–10% of cells present at the peak of the response will remain as the memory cell pool. However, it is experimentally tricky to catch the exact time of the peak of the response and, depending on immunization conditions, such as the cytokine milieu the extent of contraction varies (Badovinac et al., 2000; Blattman et al., 2003; Harty and Badovinac, 2002). For instance, in the experiments depicted in Figures 2D and 2E, the ratio between the number of memory

A

Mki67/Bcl2 co-expresion by CD127/KLRG1-defined subsets

CD127-KLRG1- (EEC)

CD127-KLRG1+ (SLEC)

CD127+KLRG1- (MPEC)

■ Mki67+Bcl2- (Early effector)
■ Mki67-Bcl2- (Late effector)
■ Mki67-Bcl2+ (Memory)

D4   D6   D8   D13   D21   D46

B

CD127/KLRG1 co-expression by Mki67/Bcl2-defined subsets

Mki67+Bcl2- (Early effector)

Mki67-Bcl2- (Late effector)

Mki67-Bcl2+ (Memory)

■ CD127-KLRG1- (EEC)
■ CD127-KLRG1+ (SLEC)
■ CD127+KLRG1- (MPEC)

D4   D6   D8   D13   D21   D46

Figure 5. Relationship between Differentiation Stages as Defined by CD127/KLRG1 or Mki67/Bcl-2 Co-expression

Naive CD45.1+ F5 TCR-tg CD8 T cells were transferred to CD45.2+ C57BL/6 congenic recipients, which were immunized the next day by intranasal infection with VV-NP68. At the indicated time points, the spleens were collected and F5 CD8 T cell responders were analyzed by flow cytometry for CD127/KLRG1/Mki67 and Bcl2 co-expression.

(A) Pie chart representation of the mean proportions of splenic early effector (red), late effector (green), and memory (purple) stages, as defined by Mki67/Bcl2 co-expression, among EEC, SLEC, and MPEC cells, as defined by CD127/KLRG1 co-expression. All pie surfaces are proportional to the size of the population at the indicated time points.

(B) Pie chart representation of the mean proportions of splenic EEC (blue), SLEC (red), and MPEC (black) stages, as defined by CD127/KLRG1 co-expression, among early effector, late effector, and memory cells, as defined by Mki67/Bcl2 co-expression. All pie surfaces are proportional to the size of the population at the indicated time points.

One representative of two independent experiments, with three to five mice in each group is shown.

improve the simulations (Figures 6D and S6D). We then questioned whether we could reduce the number of measurements and estimate parameters values from only D6, D8, and D13 experimental data. Although the effector subset dynamics were less well simulated than with five experimental points (Figure S6E), this did not affect the long-term prediction of memory cell quantities (Figure 6E). In conclusion, measuring naive, early, and late effectors, and memory cell counts, as defined by their CD44/Mki67/Bcl2 phenotype at three to five early time points (with three to five mice per group) is sufficient to correctly predict long-term memory cell counts with the NELM model.

DISCUSSION

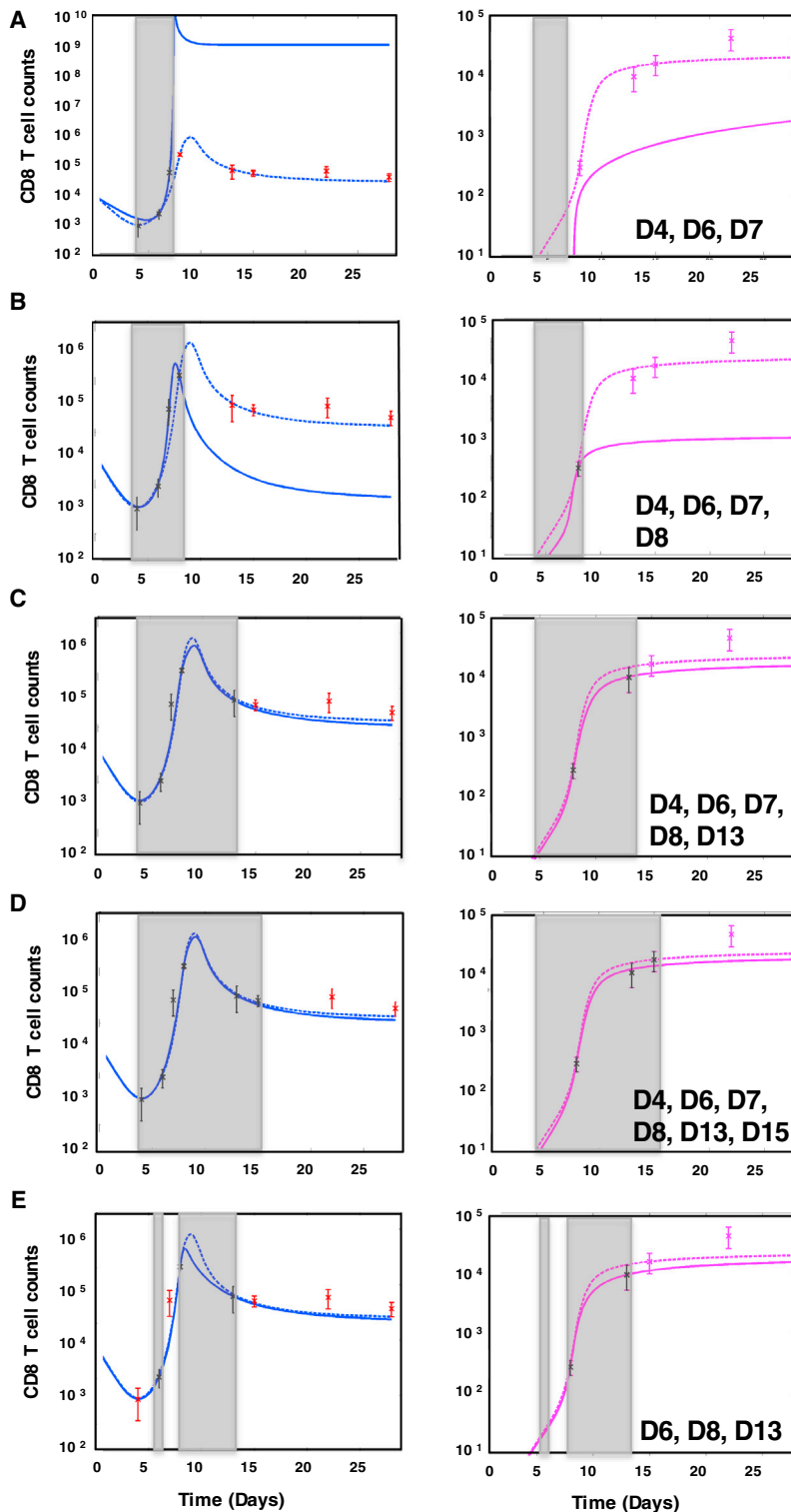The current study revisited the sequence of events accompanying the differentiation of naive CD8 T cells upon antigenic stimulation in vivo and in silico. Three independent approaches: unsupervised clustering of transcriptomics data (Figure 1), surface phenotyping (Figure 2), and mathematical modeling (Table S1) demonstrated the effector phase should be considered as a two-step differentiation stage. The identification of CD44+ Mki67+ Bcl2− early effector, CD44+ Mki67− Bcl2− late effector and CD44+ Mki67− Bcl2+ memory populations was common to TCR-Tg and non-transgenic cells, in infectious and tumoral contexts and in all tested organs (blood, spleen, draining lymph nodes, and lung). It thus represents a common feature of murine primary CD8 T cell responses. Interestingly, it matches the phenotype of day-15 effector and month-6 memory cells induced by vaccination in humans (Miller et al., 2008), and it may thus be generalized to human and possibly other species. The expression of Mki67+, a marker of cycling cells (Starborg et al., 1996), by early effector cells fits with the tremendous early expansion observed during the beginning of this phase and is in agreement with data showing that activated cells need to perform at least five cell cycles to acquire a memory generation potential (Opferman et al., 1999). The second effector stage corresponds to quiescent Mki67− cells. The functional significance of the CD44+ Mki67− Bcl2− differentiation step requires further investigation. Our preliminary results could not highlight major differences between early and late effector cells, at least in terms of cytokine production (data not shown), although a

Figure 6. Predictive Simulations of Memory CD8 T Cell Counts

(A–E) Mice were immunized by intranasal infection with vaccinia and recipients were bled at the indicated time points. Endogenous B8R-specific CD8 T cell responders were analyzed by flow cytometry for CD44, Mki67, and Bcl2 co-expression to calculate absolute numbers of total (blue, left-hand) and memory (purple, right-hand) cells (mean ± SD). The parameter values of the NELM model were estimated by fitting experimental data from: (A) D4–D7; (B) D4–D8; (C) D4–D13; (D) D4–D15; or (E) D6, D8, and D13; and cell dynamics were simulated (plain curves). Overlaid dashed curves correspond to the simulations obtained using all D4–D28 experimental data to estimate parameter values of the NELM model. Experimental time points used for fitting are inserted in graphs, displayed in black and highlighted by a shaded background.

See also Figure S6.

Bcl2 re-expression among MPEC cells at the peak of the response (Dunkle et al., 2013).

CD8 T cells have been subdivided into subsets of cells sharing a similar phenotype (Chang et al., 2014; Harty and Badovinac, 2008; Kaech and Cui, 2012). Herein, we show that such phenotypically defined subsets can represent functional classes rather than steps in a differentiation process, even when successively observed. This is the case of CD62L-based central and effector lineages (Figures 4A and 4B). Conversely, the CD127/KLRG1-based SLEC/MPEC paradigm seems to represent a true genealogy, as suggested by transfer experiments (Joshi et al., 2007) and because it can be successfully described by the corresponding dynamical model (Figure 4D). However, we confirmed that MPEC is a large, composite (in terms of Mki67/Bcl2 expression) population at the peak of the response that only slowly enriches itself in memory cells thereafter. Still, we could identify nascent memory cells among MPEC with the CD44+ Mki67– Bcl2+ discriminative phenotype. This phenotypic identification of memory cells during the effector phase will help to investigate the molecular cues regulating commitment to either cell fate.

Based on our phenotypic definition of naive, early and late effectors, and memory populations, we used mathematical modeling of cell population sizes to investigate genealogical relationships between these subsets. Indeed, transfer experiments can only assess the pres-

higher fraction of E cells express Granzyme B (Figure S2A). Emerging memory cells (CD44+ Mki67– Bcl2+) are characterized by de novo expression of the anti-apoptotic Bcl2 molecule, which fits with the long-lived potential of these cells. Interestingly, using a Bcl2-reporter mouse model, others have shown that memory differentiation potential is correlated with

ence of precursors within a given population without quantification (Hand et al., 2007; Kaech et al., 2003; Kedzierska et al., 2007). They can thus only access the destiny of cells that survive the transfer and the subsequent differentiation process, making it difficult to establish parental links between global populations. Conversely, through mathematical formalism we

can hypothesize putative genealogical trees linking phenotypically defined populations and compare their abilities to quantitatively reproduce the time evolution of population sizes, thus identifying genealogies that can explain the observed dynamics. We previously published mathematical models of primary CD8 T cell responses (Crauste et al., 2015; Terry et al., 2012) based on a three-compartment differentiation scheme. These models were adapted from those developed in seminal studies (Antia et al., 2005; De Boer et al., 2001; Ganusov, 2007), with modifications to allow a single set of ordinary differential equations to simulate total CD8 T cells counts, thanks to feedback mechanisms (Crauste et al., 2015; Terry et al., 2012). We herein modified our original models to take two effector compartments into account (Table S1 and Figure S4).

First, we found that models in which memory cells differentiate only directly from naive cells, as proposed in Buchholz et al. (2013), poorly reproduced our experimental data (Table 1) and were unable to simulate memory cell dynamics (Figures S5A and S5B), indicating that naive cells need first to differentiate into effectors before memory generation (Bannard et al., 2009). The discrepancy between the two formal approaches could result from the fact that the $T_{CM}p \rightarrow T_{EM}p \rightarrow$ effector model (Figure 4D), which does not harbor negative feedback loops, is not able to account for both expansion and contraction phases. Although it can reproduce the dynamics of populations in terms of relative sizes of the populations and total CD8 counts up to D8 of the response (Buchholz et al., 2013), it fails to simulate the contraction that occurs thereafter (Figure 4D) and hence the generation of memory cells.

Second, the NELM linear model was identified as the best model among all tested models. There has been intense debate on whether differentiation pathways are linear or branching (Arsenio et al., 2015; Flossdorf et al., 2015). In the current study, branching models either failed to describe the generation of M cells (Figure S5A and S5B) or the decay of E or L cells (Figure S5C), when L cells represent terminally differentiated cells. This extends the results obtained in initial modeling studies that showed that terminally differentiated, undividing effectors cannot explain the dynamics of CD8 T cell counts (Antia et al., 2005; Ganusov, 2007). Among models including additional N→M and/or E→M branches on top of the linear N→E→L→M genealogy (a–c) it is, however, noticeable that differentiation rates of memory cells from naive, early, or late effectors indicate that the vast majority of cells follow the linear N→E→L→M pathway. It would be interesting to identify priming conditions able to favor the differentiation of memory cells directly from naive or early effector precursors (e.g., manipulating inflammation levels [Cui et al., 2009; Harty and Badovinac, 2008]) and to characterize the properties of memory cell populations resulting from different genealogical tracks. Our results also highlight a possible branching between CD62L+ central and CD62L–effector lineages (Figure 4B) but, as CD62L-based phenotypes do not define genealogically linked differentiation stages, it is difficult to assess at which stage the branching between the two classes from CD62L+ naive cells occurs.

Importantly, we could simulate memory cell counts with the NELM model from only a few early measurements of cell subset counts. Measurements on a (D6–D13) time frame encompassing the expansion peak yield sufficient information to correctly

estimate parameter values of the model and therefore generate memory population dynamics and predict long-term memory cell counts. Thus, the NELM mathematical model allows prediction in these experimental conditions. Other experimental conditions, manipulating controllers of the response (such as antigen, route, inflammation, or knockout contexts), will need further investigation to establish the robustness and predictive capacities of the differentiation models based on CD44/Mki67/Bcl2 phenotypes.

In conclusion, we propose a dynamical model of CD8 T cell primary responses based on previously unidentified phenotypic markers that define four differentiation stages. It will facilitate precise investigations of the molecular actors and immunization conditions that control effector and memory cell generation. Its translation to mathematical formalism allows the prediction, from a few experimental measurements during the effector phase, of the quantity of memory cells that will be generated. It could thus help to reduce time and cost issues in the process of candidate vaccine screening in preclinical studies.

STAR★METHODS

Detailed methods are provided in the online version of this paper and include the following:

- KEY RESOURCES TABLE
- CONTACT FOR REAGENT AND RESOURCE SHARING
- EXPERIMENTAL MODELS
- METHOD DETAILS
  - Phenotypic Analyses
  - Cell Culture
  - Transcriptomics Data Analyses
  - Mathematical Modeling
- QUANTIFICATION AND STATISTICAL ANALYSIS
  - Results Presentation
  - Blood Cell Enumeration
  - Statistical Tests for Model Selection

SUPPLEMENTAL INFORMATION

Supplemental Information includes six figures and three tables and can be found with this article online at http://dx.doi.org/10.1016/j.cels.2017.01.014.

AUTHOR CONTRIBUTIONS

F.C. designed, wrote, and solved the mathematical models with the help of O.G. J. Mafille performed the experimental work with the help of S.D. and C.A. L.B. performed transcriptomics analyses. C.A. and J. Marvel conceived of the study and designed the experiments. C.A. and F.C. wrote the paper with the help of O.G. and J. Marvel. F.C., O.G., J. Marvel, and C.A. secured funding.

REFERENCES

Ahmed, R., Bevan, M.J., Reiner, S.L., and Fearon, D.T. (2009). The precursors of memory: models and controversies. Nat. Rev. Immunol. 9, 662–668.

Antia, R., Ganusov, V.V., and Ahmed, R. (2005). The role of models in understanding CD8+ T-cell memory. Nat. Rev. Immunol. 5, 101–111.

Appay, V., van Lier, R.A.W., Sallusto, F., and Roederer, M. (2008). Phenotype and function of human T lymphocyte subsets: consensus and issues. Cytometry A 73, 975–983.

Arsenio, J., Kakaradov, B., Metz, P.J., Kim, S.H., Yeo, G.W., and Chang, J.T. (2014). Early specification of CD8+ T lymphocyte fates during adaptive immunity revealed by single-cell gene-expression analyses. Nat. Immunol. 15, 365–372.

Arsenio, J., Kakaradov, B., Metz, P.J., Yeo, G.W., and Chang, J.T. (2015). Reply to: "CD8(+) T cell diversification by asymmetric cell division". Nat. Immunol. 16, 893–894.

Badovinac, V.P., Tvinnereim, A.R., and Harty, J.T. (2000). Regulation of antigen-specific CD8+ T cell homeostasis by perforin and interferon-gamma. Science 290, 1354–1358.

Badovinac, V.P., Porter, B.B., and Harty, J.T. (2002). Programmed contraction of CD8(+) T cells after infection. Nat. Immunol. 3, 619–626.

Bannard, O., Kraman, M., and Fearon, D.T. (2009). Secondary replicative function of CD8+ T cells that had developed an effector phenotype. Science 323, 505–509.

Baron, V., Bouneaud, C., Cumano, A., Lim, A., Arstila, T.P., Kourilsky, P., Ferradini, L., and Pannetier, C. (2003). The repertoires of circulating human CD8(+) central and effector memory T cell subsets are largely distinct. Immunity 18, 193–204.

Best, J.A., Blair, D.A., Knell, J., Yang, E., Mayya, V., Doedens, A., Dustin, M.L., and Goldrath, A.W.; Immunological Genome Project Consortium (2013). Transcriptional insights into the CD8(+) T cell response to infection and memory T cell formation. Nat. Immunol. 14, 404–412.

Blattman, J.N., Grayson, J.M., Wherry, E.J., Kaech, S.M., Smith, K.A., and Ahmed, R. (2003). Therapeutic use of IL-2 to enhance antiviral T-cell responses in vivo. Nat. Med. 9, 540–547.

Bouneaud, C., Garcia, Z., Kourilsky, P., and Pannetier, C. (2005). Lineage relationships, homeostasis, and recall capacities of central- and effector-memory CD8 T cells in vivo. J. Exp. Med. 201, 579–590.

Buchholz, V.R., Flossdorf, M., Hensel, I., Kretschmer, L., Weissbrich, B., Gräf, P., Verschoor, A., Schiemann, M., Höfer, T., and Busch, D.H. (2013). Disparate individual fates compose robust CD8+ T cell immunity. Science 340, 630–635.

Burnham, K.P., and Anderson, D.R. (2002). Information and likelihood theory: a basis for model selection and inference. In Differential Equation Modeling of HIV Viral Fitness Experiments: Model Identification, Model Selection, and Multimodel Inference, K.P. Burnham and D.R. Anderson, eds. (Springer), pp. 49–97.

Chang, J.T., Wherry, E.J., and Goldrath, A.W. (2014). Molecular regulation of effector and memory T cell differentiation. Nat. Immunol. 15, 1104–1115.

Crauste, F., Terry, E., Mercier, I.L., Mafille, J., Djebali, S., Andrieu, T., Mercier, B., Kaneko, G., Arpin, C., Marvel, J., and Gandrillon, O. (2015). Predicting pathogen-specific CD8 T cell immune responses from a modeling approach. J. Theor. Biol. 374, 66–82.

Cui, W., Joshi, N.S., Jiang, A., and Kaech, S.M. (2009). Effects of signal 3 during CD8 T cell priming: bystander production of IL-12 enhances effector T cell expansion but promotes terminal differentiation. Vaccine 27, 2177–2187.

De Boer, R.J., Oprea, M., Antia, R., Murali-Krishna, K., Ahmed, R., and Perelson, A.S. (2001). Recruitment times, proliferation, and apoptosis rates during the CD8(+) T-cell response to lymphocytic choriomeningitis virus. J. Virol. 75, 10663–10669.

de Brito, C., Tomkowiak, M., Ghittoni, R., Caux, C., Leverrier, Y., and Marvel, J. (2011). CpG promotes cross-presentation of dead cell-associated antigens by pre-CD8α+ dendritic cells [corrected]. J. Immunol. 186, 1503–1511.

Dunkle, A., Dzhagalov, I., Gordy, C., and He, Y.-W. (2013). Transfer of CD8+ T cell memory using Bcl-2 as a marker. J. Immunol. 190, 940–947.

Flossdorf, M., Rössler, J., Buchholz, V.R., Busch, D.H., and Höfer, T. (2015). CD8+ T cell diversification by asymmetric cell division. Nat. Immunol. 16, 891–893.

Ganusov, V.V. (2007). Discriminating between different pathways of memory CD8+ T cell differentiation. J. Immunol. 179, 5006–5013.

Geman, D., d'Avignon, C., Naiman, D.Q., and Winslow, R.L. (2004). Classifying gene expression profiles from pairwise mRNA comparisons. Stat. Appl. Genet. Mol. Biol 3, Article19.

Hand, T.W., Morre, M., and Kaech, S.M. (2007). Expression of IL-7 receptor alpha is necessary but not sufficient for the formation of memory CD8 T cells during viral infection. Proc. Natl. Acad. Sci. USA 104, 11730–11735.

Harty, J.T., and Badovinac, V.P. (2002). Influence of effector molecules on the CD8(+) T cell response to infection. Curr. Opin. Immunol. 14, 360–365.

Harty, J.T., and Badovinac, V.P. (2008). Shaping and reshaping CD8+ T-cell memory. Nat. Rev. Immunol. 8, 107–119.

Hurvich, C.M., and Tsai, C.-L. (1989). Regression and time series model selection in small samples. Biometrika 76, 297–307.

Jameson, S.C., Lee, Y.J., and Hogquist, K.A. (2015). Innate memory T cells. Adv. Immunol. 126, 173–213.

Joshi, N.S., Cui, W., Chandele, A., Lee, H.K., Urso, D.R., Hagman, J., Gapin, L., and Kaech, S.M. (2007). Inflammation directs memory precursor and short-lived effector CD8(+) T cell fates via the graded expression of T-bet transcription factor. Immunity 27, 281–295.

Jubin, V., Ventre, E., Leverrier, Y., Djebali, S., Mayol, K., Tomkowiak, M., Mafille, J., Teixeira, M., Teoh, D.Y.-L., Lina, B., et al. (2012). T inflammatory memory CD8 T cells participate to antiviral response and generate secondary memory cells with an advantage in XCL1 production. Immunol. Res. 52, 284–293.

Kaech, S.M., and Cui, W. (2012). Transcriptional control of effector and memory CD8+ T cell differentiation. Nat. Rev. Immunol. 12, 749–761.

Kaech, S.M., Tan, J.T., Wherry, E.J., Konieczny, B.T., Surh, C.D., and Ahmed, R. (2003). Selective expression of the interleukin 7 receptor identifies effector CD8 T cells that give rise to long-lived memory cells. Nat. Immunol. 4, 1191–1198.

Kedzierska, K., Stambas, J., Jenkins, M.R., Keating, R., Turner, S.J., and Doherty, P.C. (2007). Location rather than CD62L phenotype is critical in the early establishment of influenza-specific CD8+ T cell memory. Proc. Natl. Acad. Sci. USA 104, 9782–9787.

Kemp, R.A., Powell, T.J., Dwyer, D.W., and Dutton, R.W. (2004). Cutting edge: regulation of CD8+ T cell effector population size. J. Immunol. 173, 2923–2927.

Maiwald, T., and Timmer, J. (2008). Dynamical modeling and multi-experiment fitting with PottersWheel. Bioinformatics 24, 2037–2043.

Masopust, D., Vezys, V., Marzo, A.L., and Lefrançois, L. (2001). Preferential localization of effector memory cells in nonlymphoid tissue. Science 291, 2413–2417.

Miller, J.D., van der Most, R.G., Akondy, R.S., Glidewell, J.T., Albott, S., Masopust, D., Murali-Krishna, K., Mahar, P.L., Edupuganti, S., Lalor, S., et al. (2008). Human effector and memory CD8+ T cell responses to smallpox and yellow fever vaccines. Immunity 28, 710–722.

Murali-Krishna, K., Altman, J.D., Suresh, M., Sourdive, D.J., Zajac, A.J., Miller, J.D., Slansky, J., and Ahmed, R. (1998). Counting antigen-specific CD8 T cells: a reevaluation of bystander activation during viral infection. Immunity 8, 177–187.

Opferman, J.T., Ober, B.T., and Ashton-Rickardt, P.G. (1999). Linear differentiation of cytotoxic effectors into memory T lymphocytes. Science *283*, 1745–1748.

Plumlee, C.R., Obar, J.J., Colpitts, S.L., Jellison, E.R., Haining, W.N., Lefrançois, L., and Khanna, K.M. (2015). Early effector CD8 T cells display plasticity in populating the short-lived effector and memory-precursor pools following bacterial or viral infection. Sci. Rep. *5*, 12264.

Sallusto, F., and Lanzavecchia, A. (2001). Exploring pathways for memory T cell generation. J. Clin. Invest. *108*, 805–806.

Sallusto, F., Lenig, D., Förster, R., Lipp, M., and Lanzavecchia, A. (1999). Two subsets of memory T lymphocytes with distinct homing potentials and effector functions. Nature *401*, 708–712.

Starborg, M., Gell, K., Brundell, E., and Höög, C. (1996). The murine Ki-67 cell proliferation antigen accumulates in the nucleolar and hetero-chromatic regions of interphase cells and at the periphery of the mitotic chromosomes in a process essential for cell cycle progression. J. Cell Sci. *109*, 143–153.

Su, M.W., Walden, P.R., Golan, D.B., and Eisen, H.N. (1993). Cognate peptide-induced destruction of CD8+ cytotoxic T lymphocytes is due to fratricide. J. Immunol. *151*, 658–667.

Terry, E., Marvel, J., Arpin, C., Gandrillon, O., and Crauste, F. (2012). Mathematical model of the primary CD8 T cell immune response: stability analysis of a nonlinear age-structured system. J. Math. Biol. *65*, 263–291.

Wherry, E.J., Teichgräber, V., Becker, T.C., Masopust, D., Kaech, S.M., Antia, R., von Andrian, U.H., and Ahmed, R. (2003). Lineage relationship and protective immunity of memory CD8 T cell subsets. Nat. Immunol. *4*, 225–234.

STAR★METHODS

KEY RESOURCES TABLE

Reagent or Resource	Source	Identifier
Antibodies		
FITC-coupled anti-mouse Bcl-2	BioLegend (London, UK)	Clone BCL/10C4 Cat#633504; RRID: AB_2028394
BV605-coupled anti-mouse CD45.1	BioLegend	Clone A20 Cat#110737; RRID: AB_11204076
Alexafluor700-coupled anti-mouse CD45	BioLegend	Clone 30-F11 Cat#103128; RRID: AB_493715
BV510-coupled anti-mouse CD62L	BioLegend	Clone MEL-14 Cat#104441; RRID: AB_2561537
PerCP.Cy5.5-coupled anti-mouse Mki67	eBioscience (Paris, France)	Clone SolA15 Cat#46-5698-82; RRID: AB_11040981
PE.Cy7-coupled anti-mouse CD8	eBioscience	Clone 53.6.7 Cat#25-0081-82; RRID: AB_469584
APC-coupled anti-mouse CD27	eBioscience	Clone LG.7F9 Cat#17-0271-82; RRID: AB_469370
APC-coupled anti-mouse KLRG1	eBioscience	Clone 2F1 Cat#17-5893-82; RRID: AB_469469
PE-coupled anti-human GranzymeB	ThermoFisher Scientific (TFS, Illkirch, France)	Clone GB12 Cat#MHGB04; RRID: AB_10372671
Biotin-coupled anti-mouse CD127	eBioscience	Clone A7R34 Cat#13-1271-82; RRID: AB_466588
VioBlue-coupled anti-mouse CD44	Miltenyi (Paris, France)	Clone IM7.8.1 Cat#130-102-443
Chemicals, Peptides, and Recombinant Proteins		
NaN_3	Sigma-Aldrich (Lyon, France)	Cat#S2002
Deposited Data		
Longitudinal gene expression data of OT-I cells responding to Listeria and VSV infections	Immgen Consortium (Best et al., 2013)	https://www.ncbi.nlm.nih.gov/geo/query/acc.cgi?acc=GSE15907
Experimental Models: Cell Lines		
EL4-NP68	Dr. T.N. Schumacher (de Brito et al., 2011)	Parental strain RRID: CVCL_0255
Experimental Models: Organisms/Strains		
C57BL/6 mice	Charles River Lab. (CRL, Saint-Germain-Nuelles, France)	C57BL6/J https://www.jax.org/strain/000664
CD45.1 + C57BL/6 mice	CRL	B6.SJL-Ptprc^a Pepc^b/BoyCrl http://www.criver.com/products-services/basic-research/find-a-model/ly51-mouse
F5 CD45.1+ TCR-Tg mice	Generated by crossing in our facility (Jubin et al., 2012)	B6.SJL-Ptprc^a Pepc^b/BoyCrl-Tg(CD2-TcraF5,CD2-TcrbF5)1Kio/Jmar RRID of parental strain:MGI:3760628
VV-NP68	Sir Pr. A.J. McMichael (Jubin et al., 2012)	Parental strain: Western Reserve Vaccinia Virus UniProt Taxon: 10254
Software and Algorithms		
FlowJO	TreeStar (Ashland OR, USA)	RRID: SCR_008520
Bioconductor	2.10 release http://www.bioconductor.org/packages/2.10/BiocViews.html - ___Software	RRID:SCR_006442
tspair	BioConductor 2.10 release (Geman et al., 2004)	http://www.bioconductor.org/packages/2.10/bioc/html/tspair.html

(*Continued on next page*)

OPEN ACCESS

CellPress

Continued

Reagent or Resource	Source	Identifier
Potter-Wheel 3.1 Matlab's toolbox	MathWorks (Montbonnet, France) (Maiwald and Timmer, 2008)	http://www.potterswheel.de/; RRID: SCR_001622
Other		
FlowCount Fluorospheres	Beckman Coulter (Nyon, Switzerland)	Cat#7547053
FoxP3 TF Staining Buffer Set	eBioscience	Cat#00-5523-00
efluor780-coupled FVD	eBioscience	Cat#65-0865
PE-coupled streptavidin	BD Biosciences (Le Pont de Claix, France)	Cat#554061; RRID: AB_10053328
Dulbecco's Phosphate Buffer Saline (PBS)	TFS	Cat#14190250
Fetal Calf Serum (FCS)	BioWest (Nuaillé, France)	Cat#S1810
ACK lysis buffer	TFS	Cat#A1049201

CONTACT FOR REAGENT AND RESOURCE SHARING

Further information and requests for reagents may be directed to and will be fulfilled by Lead Contact Christophe Arpin, CIRI (INSERM-U1111/CNRS-UMR5308) (christophe.arpin@inserm.fr). VV-NP68 utilization is protected by a MTA between MRC, London, U.K. and INSERM, Bron, France, and therefore cannot be disseminated.

EXPERIMENTAL MODELS

C57BL/6 mice (C57BL6/J) and CD45.1+ C57BL/6 mice (B6.SJL-Ptprc[a]Pepc[b]/BoyCrl) were purchased from CRL. F5 TCR-tg mice recognizing the NP68 epitope were crossed to a CD45.1+ C57BL/6 background (B6.SJL-Ptprc[a]Pepc[b]/BoyCrl-Tg(CD2-TcraF5,CD2-TcrbF5)1Kio/Jmar; (Jubin et al., 2012). They have been crossed at least 13 times on the C57BL6/J background. All mice were homozygous adult 6-8-week-old at the beginning of experiments. They were healthy and housed in our institute's animal facility under Specific Pathogen-Free conditions. Age- and sex-matched littermates or provider's delivery groups, which were naive of any experimental manipulation, were randomly assigned to experimental groups and co-housed at least for one week prior to experimentation. Animals were maintained in ventilated enriched cages at constant temperature and hygrometry with 13hr/11hr light/dark cycles and constant access to 21 kGy-irradiated food and acid (pH = 3 ± 0.5) water.

$2x10^5$ naive CD8 T cells from CD45.1+ F5 mice were transferred by retro-orbital injection in, briefly 3% isoflurane-anaesthetized, 6-8-week-old congenic CD45.2+ C57BL/6 mice. The day after deeply Xylazin/Ketamin-anaesthetized recipient mice were inoculated intra-nasally with $2x10^5$ pfu of a vaccinia virus expressing the NP68 epitope (VV-NP68) and provided by Pr. A.J. McMichael; alternatively, briefly 3% isoflurane-anaesthetized recipients were subcutaneously inoculated with $2.5x10^6$ EL4 lymphoma cells expressing the NP68 epitope (EL4-NP68) and provided by Dr. T.N.M. Schumacher (de Brito et al., 2011). All experimental procedures were approved by an animal experimentation ethics committee (CECCAPP; Lyon, France), and accreditations have been obtained from French government.

METHOD DETAILS

Phenotypic Analyses
Mice were bled at intervals of at least 7 days or sacrificed for organ collection. Blood and spleen cell suspensions were cleared of erythrocytes by incubation in ACK lysis solution (TFS). Cells were then incubated with efluor780-coupled Fixable Viability Dye (eBioscience) to label dead cells. All surface stainings were then performed for 45 minutes at 4°C in PBS (TFS) supplemented with 1% FBS (BioWest) and 0.09% NaN₃ (Sigma-Aldrich). Cells were fixed and permeabilized with the Foxp3-fixation and permeabilization kit (eBioscience) before intra-cellular staining for one hour to overnight. The following mAbs(clones) were utilized: Bcl2(BCL/10C4), CD45.1(A20), CD45(30-F11) and CD62L(MEL-14) from Biolegend, Mki67(SolA15), KLRG1(2F1), CD127(A7R34), CD27(LG.7F9) and CD8(53.6.7) from eBioscience, GranzymeB(GB12) from TFS and CD44(IM7.8.1) from Miltenyi. Samples were acquired on a FACS® LSR Fortessa (BD biosciences) and analyzed with FlowJo software (TreeStar).

Cell Culture
The EL4-NP68 cell line is maintained for a maximum of 4 weeks at 37°C in 5% CO₂ incubator, in DMEM (TFS) medium supplemented with 6% FBS (BioWest), 2 mM L-glutamin, 50 g/ml gentamicin, 10 mM (pH 7.4) HEPES buffer (all from TFS), and 50 M 2-ME (Sigma-Aldrich). Cells were diluted 1/10 on Mondays and Wednesdays and 1/20 on Fridays.

Transcriptomics Data Analyses

Gene expression data from ImmGen (Best et al., 2013; https://www.immgen.org/) were recovered from Gene Expression Omnibus (http://www.ncbi.nlm.nih.gov/geo/; GEO: GSE15907). Data were processed and analyzed with R and Bioconductor (Release 2.10) packages. Samples corresponding to the kinetics of OT-I in vivo responses to VSV and *Listeria* were hierarchically clustered according to their expression profiles. Expressions throughout the four main clusters corresponding to naive (D0), early effector (D0.5-D6), late effector (D8-D15) and memory (D45-D106) phases were compared and the Top Scoring Pair method (Geman et al., 2004; *tspair* Bioconductor package) was applied to identify pairs of genes with most opposite expression patterns.

Mathematical Modeling

Models

All mathematical models assessed to fit CD44/Mki67/Bcl2 expression data (Figure S3) contain five variables denoted P for pathogen counts and N, E, L, and M for cellular counts, the dynamics of which are described by nonlinear ordinary differential equations (Figure 3C). The following general assumptions have been made:

- Naive cells differentiate only in the presence of the pathogen.
- Only Mki67+ cells proliferate (Starborg et al., 1996).
- Both Mki67- and Mki67+, Bcl2- populations (E and L) exert cytolytic functions. Indeed, both populations harbour significant intra-cellular contents of Granzyme B, as compared to M cells (Figure S2A).
- All cellular compartments and pathogen die with constant rates. The pathogen is subject to E and L cell cytoxicity, as well as E and L cells themselves to take into account competition for nutrients and fratricide killing (Kemp et al., 2004; Su et al., 1993).

The deterministic model assessed to fit CD44/CD27/CD62L expression data in Buchholz *et al.*; Figure 4C) is the almost linear differentiation sequence $T_{CM}p \rightarrow T_{EM}p \rightarrow T_{EFF}$, given by:

$$N^{'}(t) = -d_{0,1}N(t) - d_{0,2}N(t) , \qquad \text{(Equation 1)}$$

$$T^{'}_{CM}(t) = d_{0,1}N(t) + \lambda_1 T_{CM}(t) - d_1 T_{CM}(t) , \qquad \text{(Equation 2)}$$

$$T^{'}_{EM}(t) = d_{0,2}N(t) + d_1 T_{CM}(t) + \lambda_2 T_{EM}(t) - d_2 T_{EM}(t) \qquad \text{(Equation 3)}$$

$$T^{'}_{EFF}(t) = d_2 T_{EM}(t) + \lambda_3 T_{EFF}(t) . \qquad \text{(Equation 4)}$$

The mathematical model assessed to fit CD44/CD127/KLRG1 expression data (Figure 4D) was written to describe the differentiation of SLEC or MPEC, both from EEC, and is given by:

$$N^{'}(t) = -\mu_N N(t) - \delta_{NE}P(t)N(t) , \qquad \text{(Equation 5)}$$

$$E^{'}(t) = \delta_{NE}P(t)N(t) + [\rho_E P(t) - \mu_E E(t) - \delta_{ES} - \delta_{EM}]E(t) , \qquad \text{(Equation 6)}$$

$$S^{'}(t) = \delta_{ES}E(t) + [\rho_S P(t) - \mu_S S(t) - \mu_S^0]S(t) , \qquad \text{(Equation 7)}$$

$$M^{'}(t) = \delta_{EM}E(t) - \mu_M M(t) , \qquad \text{(Equation 8)}$$

$$P^{'}(t) = [\rho_P P(t) - \mu_{PS}S(t) - \mu_{PM}M(t) - \mu_P^0]P(t) . \qquad \text{(Equation 9)}$$

In all cases, the initial conditions were as follows: we assume that there is no CD44+ (E, L, M, EEC, SLEC, MPEC, $T_{CM}p$, $T_{EM}p$ and Effectors) cell prior to the infection (primary response). The initial number of CD44- cells is fixed (N(0) = 8090 cells). This value has been evaluated in several immunization models and proved to be robust. Since pathogen dynamics is normalized (Crauste et al., 2015), the initial amount of pathogen is given by P(0) = 1.

Parameter Value Estimation

All parameters are assumed to be nonnegative and those associated with differentiation are positive. We fitted experimental data and estimated parameter values with PottersWheel (Maiwald and Timmer, 2008) Matlab's toolbox (MathWorks). All data are fitted

OPEN
ACCESS

CellPress

simultaneously. To compare the abilities of three- and four-compartment models to describe a single effector population, E and L populations are summed up before fitting (Table S1). Thus, the objective is to minimize the χ^2 function defined by

$$\chi^2(p) = \chi^2_N(p) + \chi^2_{EFF}(p) + \chi^2_M(p), \qquad \text{(Equation 10)}$$

where

$$\chi^2_X(p) = \sum_{i=1}^{T} \left(\frac{\overline{x}_i - X(t_i, p)}{\sigma_i} \right)^2 , \qquad \text{(Equation 11)}$$

with $X = N$ (CD44-Mki67-Bcl2+), EFF (CD44+Bcl2-), or M (CD44+Mki67-Bcl2+), and p being the set of parameters that are estimated, $\overline{x}_i$ the i-th observation of X (which is here a mean value), σ_i the standard deviation of X at $t = t_i$, and T the number of experimental points.

We also fitted all 4-compartment models with E and L populations separately (Table 1), the objective thus being to minimize the χ^2 function defined by:

$$\chi^2(p) = \chi^2_N(p) + \chi^2_E(p) + \chi^2_L(p) + \chi^2_M(p). \qquad \text{(Equation 12)}$$

The initial models, consisting in the description of a given differentiation pathway and including all realistic proliferation and death processes that could be considered (Figure 3B), have been gradually simplified by progressively eliminating negligible parameters, as long as the χ^2 values improved and the differentiation pathway was preserved.

QUANTIFICATION AND STATISTICAL ANALYSIS

Results Presentation
Where depicted, graph bars describe means ± standard deviation.

Blood Cell Enumeration
The volume of sampled blood (V_S) was precisely measured and a given number (F) of FlowCount Fluorospheres (Beckman Coulter) was added to each sample. The ratio between the numbers of FACS-analyzed CD8 T cell responders (R_{FACS}) and fluorospheres (F_{FACS}) was then used to recalculate the concentration of CD8 T cell responders in the blood (C_R), considering:

$$C_R = \frac{F}{V_S} \times \frac{R_{FACS}}{F_{FACS}} , \qquad \text{(Equation 13)}$$

and total numbers of circulating cells were calculated considering 2 mL of blood per mouse.

Statistical Tests for Model Selection
To compare models with different numbers of parameters, we used the corrected Akaike information criterion (Hurvich and Tsai, 1989) to avoid selection of over-parameterized models:

$$\text{AICc} = 2p - 2\log(L) + \frac{2p(p+1)}{s-p-1} = 2p + \chi^2 - 2\log(C) + \frac{2p(p+1)}{s-p-1} , \qquad \text{(Equation 14)}$$

where p is the number of parameters, L the likelihood (expressed as a function of χ^2 and a constant C depending on the sample), and s the size of the experimental sample.

In order to compare models based on their AICc values, we computed Δ_i values, defined as

$$\Delta_i = \text{AICc}_i - \text{AICc}_{min}, \qquad \text{(Equation 15)}$$

and Akaike weights w_i (Burnham and Anderson, 2002), given by

$$w_i = \frac{\exp(-\Delta_i/2)}{\sum_j \exp(-\Delta_j/2)} , \qquad \text{(Equation 16)}$$

that provide "weight of evidence" in favor of a model and can be interpreted as probabilities for a given model to be the best for the data, given the data and a set of models (Burnham and Anderson, 2002).

Supplemental Information

Identification of Nascent Memory CD8

T Cells and Modeling of Their Ontogeny

Fabien Crauste, Julien Mafille, Lilia Boucinha, Sophia Djebali, Olivier Gandrillon, Jacqueline Marvel, and Christophe Arpin
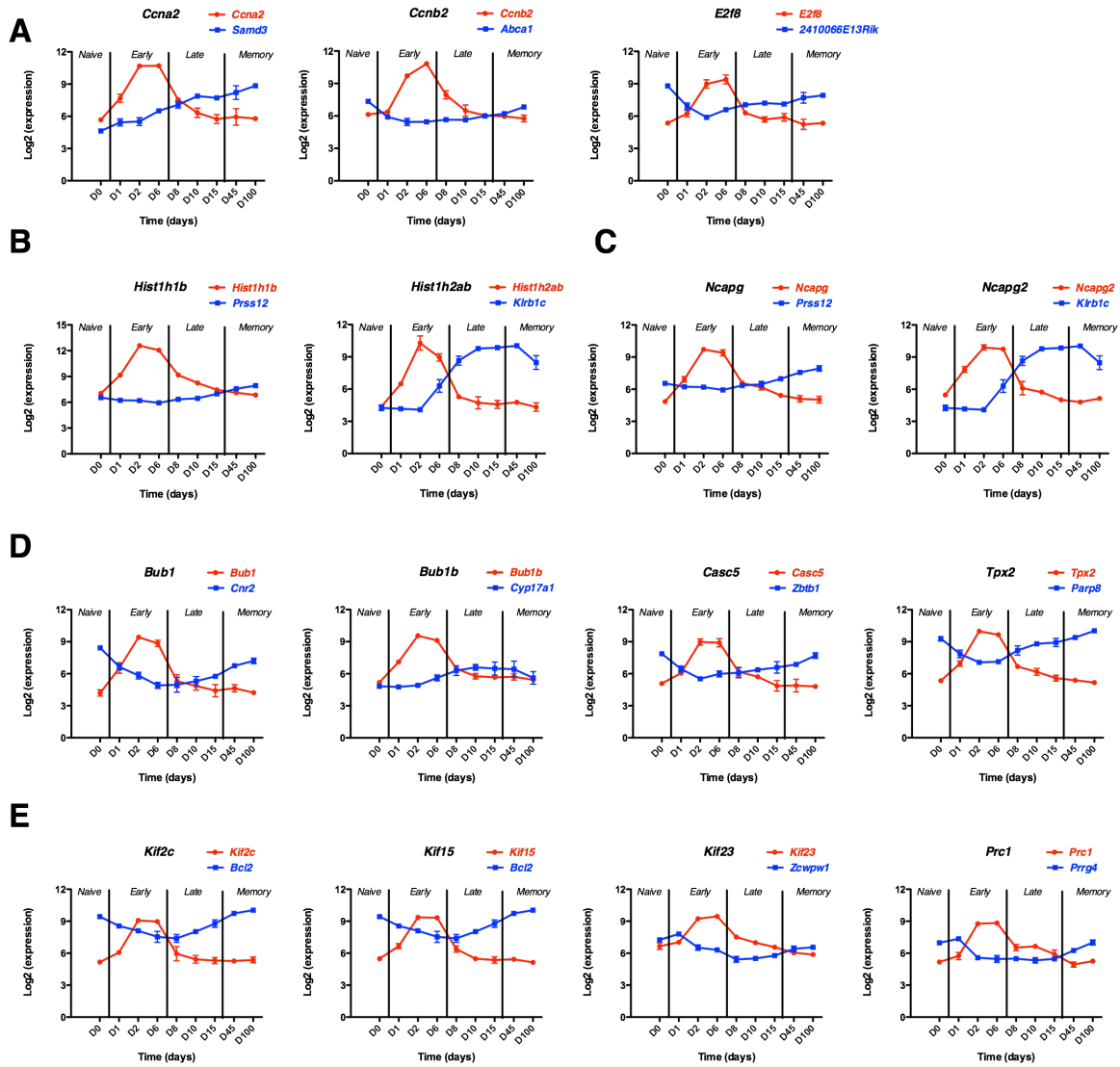
Figure S1. Related to Figure 1. Expression profiles of molecules potentially involved in cell cycle and up-regulated during the early stage of the effector phase.

Analysis of longitudinal Immgen consortium's transcriptomics data from spleen OT-I CD8 T cells at D1, D2, D6, D8, D10, D15, D45 and D100 after Lis-OVA infections were analyzed by a top scoring pair approach (Geman et al., 2004). Depicted is the expression level (mean ± SEM) of a selection of genes specifically up-regulated during the early stage of the effector phase (red curves) and of their best opposite partners (blue curves), showing early and transitory up-regulation of molecules involved in either cell cycle progression (A), chromatin organization (B), mitotic chromosome condensation (C), spindle assembly and organization (D), and kinesin or kinesin binding (E). Vertical bars mark boundaries between naive, early effector, late effector and memory phases, as determined by the clustering in Figure 1A.

A

B
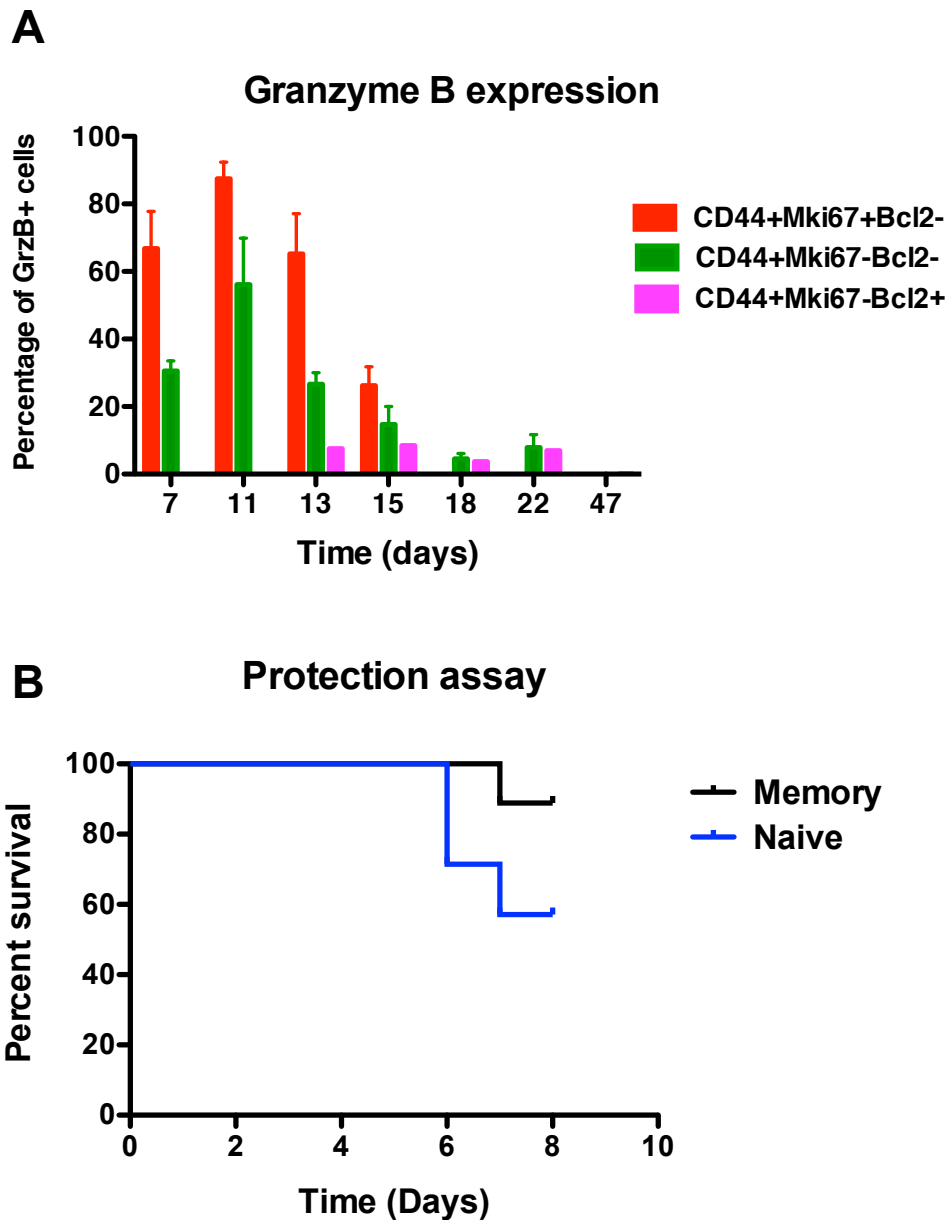
Figure S2. Related to Figure 2. Functional assessment of antigen-primed, Mki67/Bcl2-defined subsets.
Naive CD45.1+ F5 TCR-tg CD8 T cells were transferred to CD45.2+ C57BL/6 congenic recipients that were immunized the next day by intra-nasal infection with VV-NP68.
(A) Expression of Granzyme B. At the indicated time points, mice were bled and endogenous F5 CD8 T cell responders were analyzed by flow cytometry for CD44, Mki67 and Bcl2 co-expression and intra-cellular Granzyme B content of CD44+ subsets defined by Mki67/Bcl2 co-expression. One representative out of 4 experiments with 3 to 5 mice per group is shown (mean ± SD).
(B) Cross-protective capacity against an *influenza* infection. Four months after infection, F5 memory CD8 T cells (over 98% CD44+Mki67-Bcl2+) were purified by FACS-sorting and 1.2×10^5 cells were transferred to secondary hosts (black curve), in parallel with recipients receiving the same amount of naive F5 cells (blue curve). Recipients were infected the next day with a semi-lethal (10^6 TCID$_{50}$) dose of an *influenza* H1N1 virus expressing NP68 and monitored by daily weighing. In this transfer context, where no other actors of the adaptive immunological memory, such as neutralizing antibodies, are present, the protective capacities of memory CD8 T cells is specifically and stringently assessed. Animals were culled when losing over 20% of their initial weight and survival curves are shown. One representative out of 3 experiments with 8 to 15 mice per group is shown.
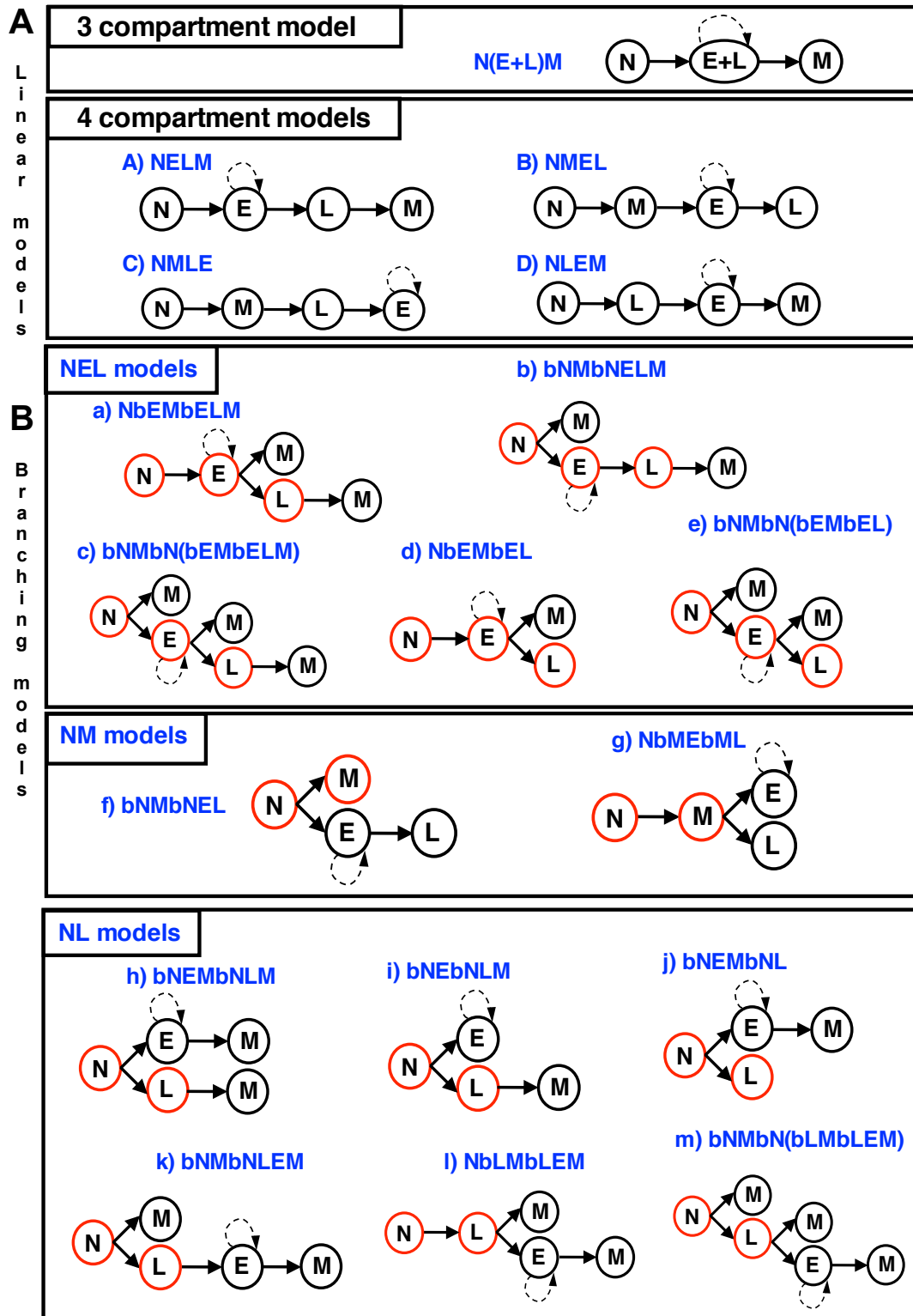
Figure S3. Related to Figures 3, S4 and S5 and all Tables. Schematic representation of the differentiation pathways mathematically modeled.

Differentiation pathways between N(=CD44-Mki67-Bcl2+), E(=CD44+Mki67+Bcl2-), L(=CD44+Mki67-Bcl2-) and M(=CD44+Mki67-Bcl2+) cellular compartments are represented by plain arrows. Circular dotted arrows depict proliferation and red circles represent common backbones in a group of branching models. Names of models in blue depict the differentiation pathways, e.g. NLEM correspond to the N→L→E→M pathway. Each branch in the names is described starting with b, e.g. NbMEbML depicts N→M, followed by either M→E or M→L.

Linear models (A). Branching models (B). See Tables 1, S1 and S2 for comparisons of the different models.
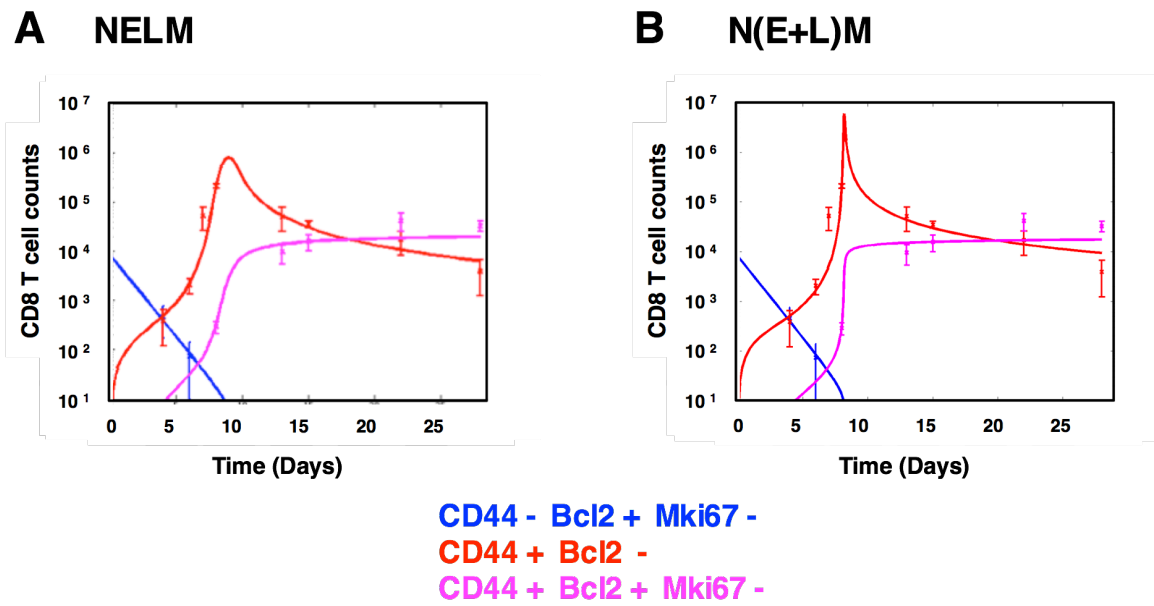
Figure S4. Related to Figures 1 and S3A and Table S1. Representation of the simulations from the best fits of NELM and N(E+L)M models.

Mice were immunized by intra-nasal infection with vaccinia and recipients were bled at the indicated time points. Endogenous B8R-specific CD8 T cell responders were analyzed by flow cytometry for CD44, Mki67 and Bcl2 co-expression. Plain lines represent the simulated (Blue, N = CD44-Mki67-Bcl2+; Red, E+L = CD44+Bcl2-; Purple, M = CD44+Mki67-Bcl2+) populations and points with SD error bars the experimental data. Best fits of the N→E→L→M four- (A) and N→(E+L)→M three- (B) compartment models.
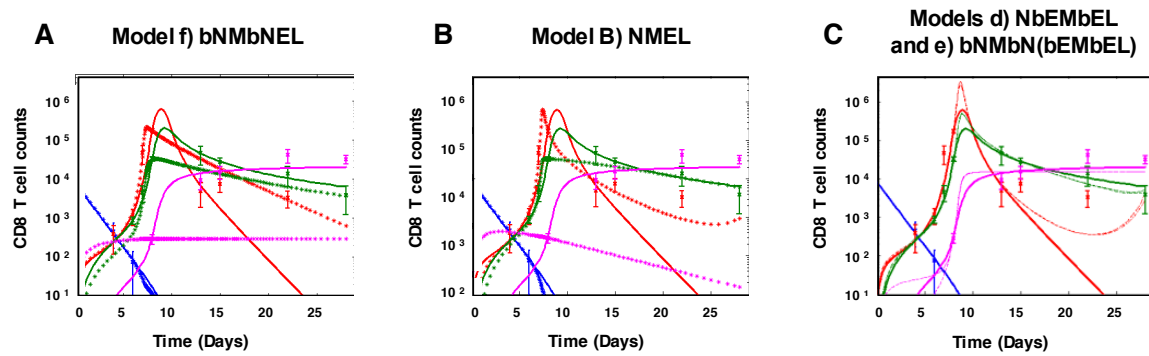
Figure S5. Related to Figures 3A and S3, and Tables 1 and S3. Simulations yielded by the best fits of models with a terminal L compartment compared to those from the NELM model.

Mice were immunized by intra-nasal infection with vaccinia and recipients were bled at the indicated time points. Endogenous B8R-specific CD8 T cell responders were analyzed by flow cytometry for CD44, Mki67 and Bcl2 co-expression to calculate absolute cell numbers (mean ± SD). Parameter values were then estimated by fitting experimental counts of naive (blue), early effector (red), late effector (green) and memory (purple) subsets. NELM (plain lines) is compared to alternative differentiation pathways:

(A) bNMbNEL model (**f**), starry lines

(B) NMEL model (**B**), starry lines

(C) NbEMbEL model (**d**), and bNMbN(bEMbEL) model (**e**), dotted lines.
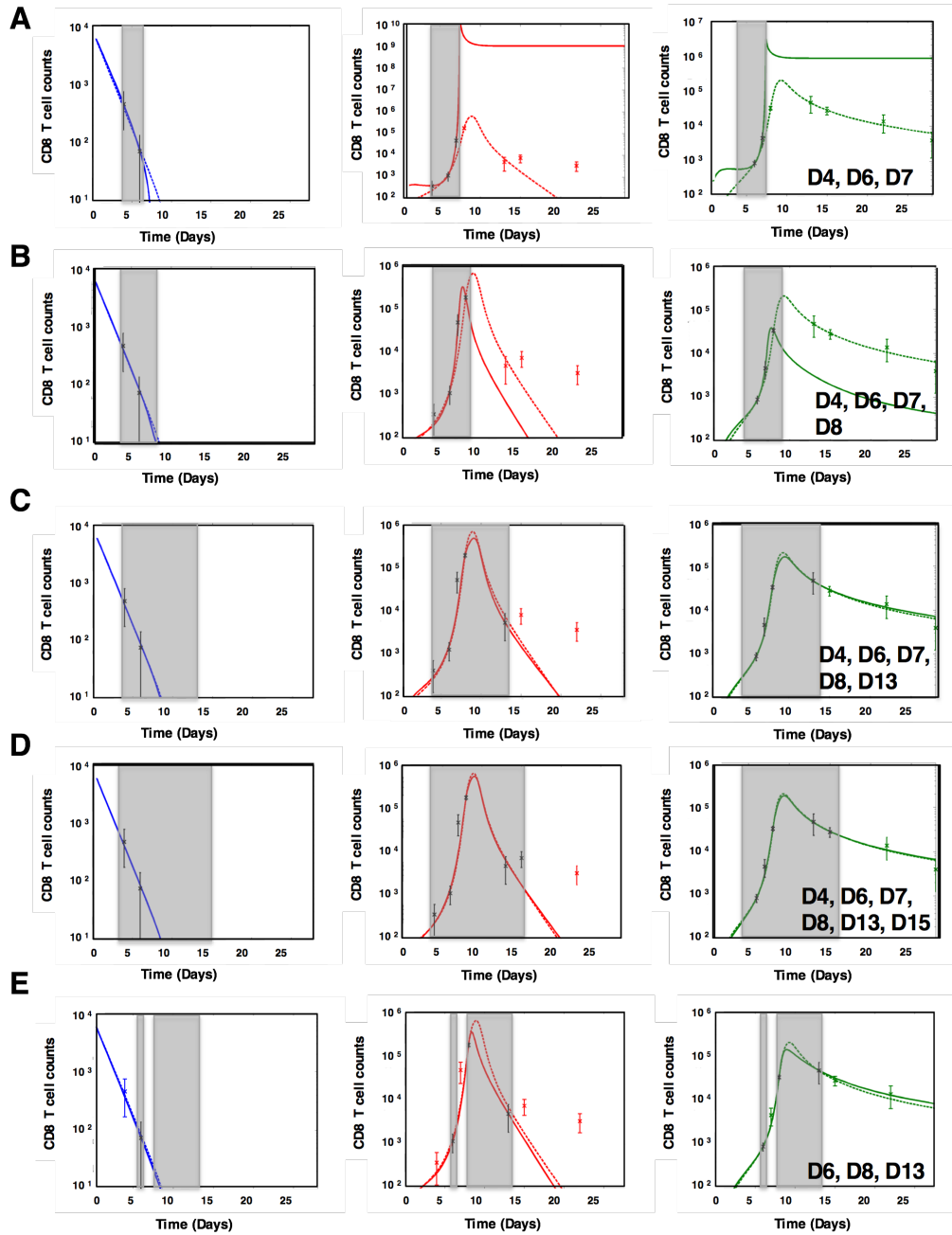
Figure S6. Related to Figure 6. Simulation of naive and effector subsets dynamics with the NELM model fitted using different experimental value sets.

Mice were immunized by intra-nasal infection with vaccinia and recipients were bled at the indicated time points. Endogenous B8R-specific CD8 T cell responders were analyzed by flow cytometry for CD44, Mki67 and Bcl2 co-expression to calculate absolute numbers of naive (blue, left-hand), early effector (red, center) and late effector (green, right-hand) cells (mean ± SD). The NELM model's parameter values were estimated by fitting experimental data from: (A) D4-D7; (B) D4-D8; (C) D4-D13; (D) D4-D15; or (E) D6, D8 and D13; and subset dynamics were simulated (plain curves). Overlaid dotted curves correspond to the simulations obtained using all D4-D28 experimental data to estimate NELM model's parameter values. Experimental time points used for fitting are inserted in graphs, displayed in black and highlighted by a shaded background.

Table S1. Related to Figures 1, S3A and S4

Comparative analysis of Naive→Effector→Memory linear models with three- and four-compartments.

Model[a]	#par.[b]	$\chi^{2\,c}$	χ^2_N	χ^2_{EFF}	χ^2_M	AICc[d]
3 compartment model						
N(E+L)M[e]	8	17.1	0.1	9.1	7.9	**321**
4 compartment model						
NELM[e]	9	**3.5**	0.1	2.3	1.0	**321**

For distances between best simulations and biological data (χ^2 values) and the statistical test (AICc) the smaller the value, the better the model. Best values are shown in bold. See Experimental Procedures for χ^2 and AICc calculations.

[a]: Schematic representations are given in Figure S3A.
[b]: Number of significant parameters.
[c]: $\chi^2 = \chi^2_N + \chi^2_{EFF} + \chi^2_M$.
[d]: AICc is for corrected Akaike Information Criterion (Hurvich and Tsai, 1989).
[e]: Names correspond to those given in Figure S3A and are explained in its legend.

Table S2. Related to Figures 2D and 3A.

Comparative analysis of the 6 top models in Figure 3A in their ability to fit the data depicted in Figure 2D of the F5 response to a tumor immunization.

Model[a]	#par.[b]	χ^{2} [c]	χ^{2}_{N}	χ^{2}_{E}	χ^{2}_{L}	χ^{2}_{M}	AIC[d]	Δ_{i}[d]	w_{i}[d]
A)[e]=NELM	9	4.7	0	1.1	3.1	0.5	**348**	**0**	**99.3**
f)[e]=bNMbNEL	9	14.7	0	4.5	5.7	4.5	358	10	0.7
B)[e]=NMEL	10	11.8	0.1	1.2	5.8	4.7	487	139	0
a)[e]=NbEMbELM	10	4.6	0	1.1	3.2	0.3	479	131	0
b)[e]=bNMbNELM	10	4.8	0	1.2	3.0	0.5	480	132	0
d)[e]=NbEMbEL	10	**1.6**	0	0.9	0.5	0.3	476	128	0

For distances between best simulations and biological data (χ^{2} values) and the statistical test (AICc) the smaller the value, the better the model. Best values are shown in bold. See Experimental Procedures for χ^{2}, AICc and w_{i} calculations.

a: Schematic representations are given in Figure S3.
b: Number of significant parameters.
[c]: $\chi^{2} = \chi^{2}_{N}+\chi^{2}_{E}+\chi^{2}_{L}+\chi^{2}_{M}$.
[d]: AICc is for corrected Akaike Information Criterion (Hurvich and Tsai, 1989), Δ_{i} is the difference between the minimal value of AICc (here 348) and model's value; and w_{i} are the Akaike weights (Burnham and Anderson, 2002), in percentages.
[e]: Names correspond to those given Figure S3A and are explained in its legend.

Table S3. Related to Figures 3, S3 and S5 and to Table 1.

Values of parameters yielding the best fit of experimental data by the top six models.

Parameter[a]	Unit	Model A)[b] NELM Rank 1[c]	Model f)[b] bNMbNEL Rank 2[c]	Model B)[b] NMEL Rank 3[c]	Model a)[b] NbEMbELM Rank 4[c]	Model b)[b] bNMbNELM Rank 5[c]	Model d)[b] NbEMbEL Rank 6[c]
μ_N	d^{-1}	0.75	0.69	0.68	0.75	0.75	0.74
δ_{NE}	d^{-1}	0.009	0.015	n.a.[d]	0.009	0.009	0.011
δ_{NM}	d^{-1}	n.a.[d]	0.023	0.052	n.a.[d]	10^{-3} [e]	n.a.[d]
ρ_E	d^{-1}	0.64	0.42	0.53	0.65	0.64	0.68
μ_{EE}	10^{-6} cell^{-1}d^{-1}	21.5	4.4	19.5	5.8	21.5	0
μ_{EL}	10^{-6} cell^{-1}d^{-1}	0	0	0	1.5	0	9.6
δ_{EM}	d^{-1}	n.a.[d]	n.a.[d]	n.a.[d]	10^{-4} [e]	n.a.[d]	$6.3\ 10^{-3}$
δ_{EL}	d^{-1}	0.59	0.47	0.62	0.63	0.59	0.69
μ_{LE}	10^{-8} cell^{-1}d^{-1}	3.6	0	**1756.3**	3.7	3.6	23
μ_{LL}	10^{-6} cell^{-1}d^{-1}	7.5	8.7	0	7.3	7.5	5.2
μ_L	d^{-1}	0	0	0.14	0	0	0.16
δ_{LM}	d^{-1}	0.025	n.a.[d]	n.a.[d]	0.026	0.025	n.a.[d]
μ_M	d^{-1}	0	0	0	0	0	0
δ_{ME}	d^{-1}	n.a.[d]	n.a.[d]	0.147	n.a.[d]	n.a.[d]	n.a.[d]
ρ_P	d^{-1}	0.15	0.14	0.20	0.13	0.15	0.12
μ_{PE}	10^{-7} cell^{-1}d^{-1}	1.8	0	**134.6**	2.4	1.8	6.1
μ_{PL}	10^{-5} cell^{-1}d^{-1}	1.8	15.6	0	1.4	1.8	0.3
μ_P	10^{-2} d^{-1}	5.5	0.14	0.11	1.9	5.5	0.7

Each model was fitted to experimental data with PottersWheel (Maiwald and Timmer, 2008) Matlab's toolbox that simultaneously fits all cellular compartments (See Experimental Procedures). The values of the parameters leading to the smallest χ^2 values are presented. The differentiation rates towards M cells are shown in red and outlier, un-physiological values in bold.

[a]: μ_X is the natural death rate of X cells. μ_{XY} is the death rate coefficient of X cells under the influence of Y cells (the death rate of X cells is then $\mu_{XY}Y$). δ_{XY} is the differentiation rate of X cells into Y cells. ρ_X is the proliferation rate of X cells.

[b]: See Figures 3A or S3

[c]: see Table 1

[d]: Not applicable

[e]: Lowest value allowed by the fitting procedure